# SLC13A5/NaCT overexpression causes disrupted white matter integrity and an autistic-like phenotype

Michael J. Rigby,[1,2,3] Nicola Salvatore Orefice,[1,2] Alexis J. Lawton,[4,†] Min Ma,[5,†] Samantha L. Shapiro,[1,2] Sue Y. Yi,[3] Inca A. Dieterich,[1,2,3] Alyssa Frelka,[6] Hannah N. Miles,[5] Robert A. Pearce,[6] John Paul J. Yu,[7] Lingjun Li,[5] John M. Denu,[4] Luigi Puglielli[1,2,8]

[†]**These authors contributed equally to this work.**

1 Department of Medicine, University of Wisconsin-Madison, Madison, WI, 53705, USA

2 Waisman Center, University of Wisconsin-Madison, Madison, WI, 53705, USA

3 Neuroscience Training Program, University of Wisconsin-Madison, Madison, WI, 53705, USA

4 Department of Biomolecular Chemistry and the Wisconsin Institute for Discovery, University of Wisconsin-Madison, Madison, WI, 53715, USA

5 School of Pharmacy and Department of Chemistry, University of Wisconsin-Madison, Madison, WI, 53705, USA

6 Department of Anesthesiology, University of Wisconsin-Madison, Madison, WI, 53705, USA

7 Department of Radiology, University of Wisconsin School of Medicine and Public Health, Madison, WI, 53705, USA

8 Geriatric Research Education Clinical Center, Veterans Affairs Medical Center, Madison, WI, 53705, USA

Correspondence to: Luigi Puglielli

University of Wisconsin-Madison, Waisman Center, 1500 Highland Ave, Madison, WI 53705, USA

lp1@medicine.wisc.edu

**Short title**: SLC13A5/NaCT overexpression and autism

# Abstract

Endoplasmic-reticulum-based $N^{\varepsilon}$-lysine acetylation serves as an important protein quality control system for the secretory pathway. Dysfunctional endoplasmic reticulum-based acetylation, as caused by overexpression of the acetyl coenzyme A transporter AT-1 in the mouse, results in altered glycoprotein flux through the secretory pathway and an autistic-like phenotype. AT-1 works in concert with SLC25A1, the citrate/malate antiporter in the mitochondria, SLC13A5, the plasma membrane sodium/citrate symporter, and ATP citrate lyase (ACLY), the cytosolic enzyme that converts citrate into acetyl coenzyme A.

Here, we report that mice with neuron-specific overexpression of SLC13A5 exhibit autistic-like behaviors with a jumping stereotypy. The mice displayed disrupted white matter integrity and altered synaptic structure and function. Analysis of both the proteome and acetyl-proteome revealed unique adaptations in the hippocampus and cortex, highlighting a metabolic response that likely plays an important role in the SLC13A5 neuron transgenic phenotype.

Overall, our results support a mechanistic link between aberrant intracellular citrate/acetyl coenzyme A flux and the development of an autistic-like phenotype.

**Keywords:** citrate, acetyl-CoA, SLC13A5, AT-1, lysine acetylation

**Abbreviations:** ACLY = ATP citrate lyase; ADHD = Attention Deficit/Hyperactivity Disorder; AFU = arbitrary fluorescence units; ASD = autism spectrum disorder; DiLeu = dimethylated leucine; DIV = days *in vitro*; DTI = diffusion tensor imaging; DTT = dithiothreitol; DWI = diffusion weighted imaging; EIEE25 = early infantile epileptic encephalopathy-25; ER = endoplasmic reticulum; EtOH = ethanol; FA = fractional anisotropy; FC = fear conditioning; FDR = false discovery rate; fEPSP = field excitatory postsynaptic potentials; GO = gene ontology; HPLC = high-performance liquid chromatograph; LC-MS/MS = liquid chromatography-tandem mass spectrometry; INDY = I'm Not Dead Yet; KEGG = Kyoto Encyclopedia of Genes and Genomes; LD = light-dark; LTD = long-term depression; LTP = long-term potentiation; MB = marble burying; MD = mean diffusivity; MEA = multi-electrode array; NA = numerical aperture; NaCT = sodium/citrate co-transporter; NMDA = *N*-methyl-*D*-aspartate; NODDI = Neurite Orientation Dispersion and Density Imaging; NOR = novel object recognition; ODI = orientation dispersion index; OF = open field; ORA = overrepresentation analysis; nTg = neuron transgenic; PFA = paraformaldehyde; PO =

propylene oxide; ROI = region of interest; SD = standard deviation; SEM = standard error of the mean; SI = social interaction; TEM = transmission electron microscopy; TBSS = tract-based spatial statistics; TCA = tricarboxylic acid cycle; TFCE = threshold-free cluster enhancement; WT = wild-type

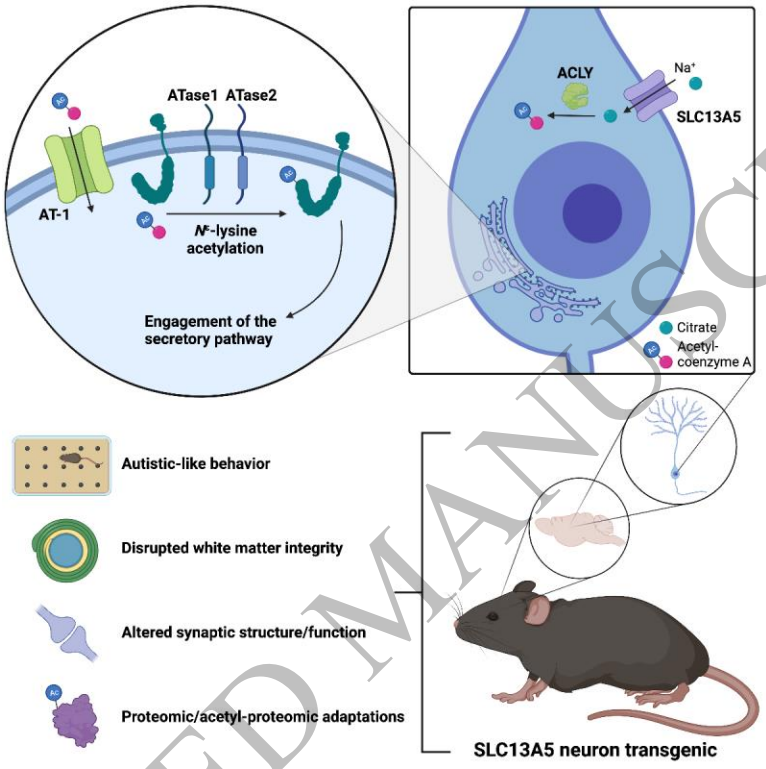


**Graphical Abstract**
**102x102 mm (0.6 x DPI)**

# Introduction

Generation and maintenance of neuronal synapses require an efficient and properly functioning secretory pathway in order to deliver the necessary proteins such as neurotransmitter receptors and ion channels. Therefore, quality control measures are vitally important in order to ensure proper function of the proteins delivered to the synapse. $N^{\varepsilon}$-lysine acetylation within the endoplasmic reticulum (ER) serves as an important protein quality control system within the secretory pathway that (1) positively selects properly folded glycoproteins, and (2) regulates the induction of reticulophagy (ER-specific autophagy) to dispose of misfolded aggregates.[1-21] Imbalanced ER-based $N^{\varepsilon}$-lysine acetylation profoundly alters glycoprotein flux through the secretory pathway, which impacts multiple organelles beyond the ER including the nucleus, mitochondria, and lysosomal network.[11,14,18-20] Aberrant ER-based $N^{\varepsilon}$-lysine acetylation can result in multiple disease states in the nervous system.[3,7,10,11,15-17,22,23] For example, loss-of-function mutations in the ER acetyl-CoA transporter *AT-1/SLC33A1* are causative of hereditary spastic paraplegia 42 and are also associated with developmental disability and premature death. [22,23] On the other hand, gene duplication events of 3q25.31 containing *AT-1/SLC33A1* are associated with autism spectrum disorder (ASD), dysmorphism, and intellectual disability.[24] Mouse models with these genetic aberrations recapitulate the associated human diseases.[10,11,15]

We recently reported that overexpression of AT-1/SLC33A1 in mouse forebrain neurons, termed the AT-1 neuron transgenic (nTg), resulted in an autistic-like phenotype with increased dendritic branching and spine formation, altered synaptic plasticity, and significant upregulation of proteins involved in synaptic generation and maintenance.[11] This phenotype was attributed to changes in glycoprotein flux through the secretory pathway due to the increased flux of acetyl-CoA from the cytosol into the ER, which altered $N^{\varepsilon}$-lysine acetylation. In order to replenish the cytosolic acetyl-CoA, AT-1 overexpressing neurons upregulated SLC25A1/CIC, the mitochondrial citrate/malate exchanger, and ATP citrate lyase (ACLY), the cytosolic enzyme that converts citrate into acetyl-CoA.[11] Thus, the neuron adapted in order to maintain the flux of cytosolic acetyl-CoA into the ER, revealing a coordinated metabolic pathway. In addition to *AT-1/SLC33A1*, gene duplication events of 22q11.21 (containing *SLC25A1*), 17q21.2 (containing *ACLY*), and 17p13.1 (containing *SLC13A5*) are all associated with ASD.[24] SLC13A5, also known as the sodium/citrate co-transporter (NaCT) or I'm Not Dead Yet (INDY), is a plasma membrane symporter that couples transport of extracellular dicarboxylate and tricarboxylates, mostly citrate, with 4 $Na^+$ cations.[25] Therefore, there appears to be a strong association between the development of ASD and aberrant intracellular citrate/acetyl-CoA flux within the cell, of which changes in ER-based $N^{\varepsilon}$-lysine acetylation likely plays an important role. As such, we hypothesized that modulating intracellular flux of citrate through overexpression of SLC13A5 would result in an autistic-like phenotype in the mouse, reminiscent of the AT-1 nTg mouse.

Here, we describe the generation and phenotypic characterization of a new mouse model that overexpresses SLC13A5 within forebrain neurons, using the same transgenic system as the previously reported AT-1 nTg autistic-like model. This SLC13A5 nTg mouse exhibits autistic-like behaviors with a jumping stereotypy, with evidence of disrupted white matter integrity, altered synaptic plasticity, and widespread changes in the proteome and acetyl-proteome. Therefore, we conclude that aberrant

intracellular flux of citrate/acetyl-CoA within the neuron is a mechanistic driver for the development of an autistic-like phenotype.

# Materials and methods

## Transgenic mouse generation

Camk2a-tTA;TRE-SLC13A5 (referred to as SLC13A5 nTg) mice were generated as previously described.[11] Briefly, human cDNA was isolated by PCR from SLC13A5-pCMV6 plasmid (Origene; RC211155) and subcloned into pTRE-Tight plasmid (Takara Bio, Inc.) using EcoRI and HindIII restriction sites. pTRE-Tight-SLC13A5 plasmid was linearized with XhoI and injected into C57BL/6J mice (The Jackson Laboratory; Stock No. 000664). Monogenic offspring were crossed with B6.Cg-Tg(Camk2atTA)1Mmay/DboJ (Camk2a-tTA) mice (The Jackson Laboratory; Stock No. 007004) to generate SLC13A5 neuron transgenic (nTg) mice. Genotyping from tail DNA was performed with the following primers: SLC13A5 forward (5'-CTTTGTGGCCACCCTGCTATTC-3'), SLC13A5 reverse (5'-AGCAAATTCGCCCCCTAGTA-3'), Camk2a-tTA forward (5'-CGCTGTGGGGCATTTTACTTTAG-3'), and Camk2a-tTA reverse (5'-CATGTCCAGATCGAAATCGTC-3').

## Animals

Mice were housed in standard cages provided by the University Laboratory Animal Resources and grouped with 1-5 littermates per cage. Animals were supplied standard chow and water *ad libitum*. All animal experiments were performed in accordance with the National Institutes of Health Guide for the Care and Use of Laboratory Animals approved by the Institutional Animal Care and Use Committee of the University of Wisconsin-Madison (protocol #M005120). SLC13A5 nTg mice used throughout the study were heterozygous for both the TRE-SLC13A5 and the Camk2a-tTA transgenes. Non-transgenic, wild type (WT) littermates were used as controls throughout the study. The specific age and sex of animals used for experiments are noted in the figure legends.

## Behavior testing

All behavioral assays were conducted within the Waisman Center Behavioral Testing Service (Madison, WI, USA) with the experimenter blind to the genotype of the mice during testing. A 30-minute acclimation period in the testing room was performed prior to each behavior assay. The following behavioral assays have been previously described[11]: marble burying assay, novel object recognition, social interaction, and fear conditioning paradigm.

### Open field exploration

Each mouse was removed from its home cage and placed in the center of the arena and allowed to explore for a duration of 30 minutes. Each mouse received one open field session. The Omnitech

Fusion system with photobeams continuously monitored and recorded the animal's placement during exploration. Quantified parameters included total distance traveled (cm), vertical activity episode count, total ambulation time (sec), and distance traveled in the centroid (cm). Data were recorded using the Omnitech Fusion system with a center ratio zone map.

### Light/dark exploration

Each mouse was placed into a split arena for a 10-minute assay. Each mouse received one session. Time spent (sec) and number of entries into the light and dark portions of the arena were recorded.

### Jumping activity

Videos were taken during the dark cycle with mice in their home cages using a red light for visualization. During each bout of jumping, the number of jumps per mouse was quantified in a 50-second time window.

## Primary neuron culturing

Primary neurons were harvested, cultured, and stained as previously described[11] on microdissected cortex and hippocampus; cultures were maintained for a maximum duration of 28 days. For immunocytofluorescence analysis of synapse formation, the following primary antibodies were used: Syn-1 (Cell Signal Technologies; 5927S; 1:200), Homer1 (Synaptic Systems; 160-011; 1:100), Psd-95 (Thermo Fisher; MAI-045; 1:500), Vglut2 (Synaptic Systems; 135-043; 1:500), and NF-200 (Thermo Fisher; PA3-16753; 1:1,000). Images were collected on a Nikon A1 inverted confocal microscope using NIS-Elements AR version 5.11.01 software with 405 nm (blue channel), 488 nm (green channel), 561 nm (red channel), and 640 nm (far red) laser wavelengths with the Galvano scan head. Multi-z-stack images (1024 × 1024 pixels with 25 z-steps every 0.15 μm) were acquired using a 60x oil objective (NA = 1.4; 0.21 μm/pixel) at a pinhole size of 39.59 μm. Neurons and neurites were identified by positive NeuN and NF-200 staining, respectively. The .nd2 images were imported into Imaris (Bitplane; Version 9.5) and converted to native .ims format. For neuron morphology, the Filament Tracer module with the Autopath method was used to trace dendrites starting from the soma with a thinnest diameter of 1.5 μm; dendrite seed points were removed within 30 μm of the soma. Dendritic spines were subsequently detected with a seed point diameter of 0.7 μm and maximum length of 7 μm. A Sholl analysis with 1 μm-spaced spheres was used to quantify dendritic branching. For assessment of synapse formation, signal from the nucleus was first removed by masking the pre- and post-synaptic marker channels using a surface reconstruction of the DAPI signal (setting voxels within the surface to zero). Two micron diameter spots were fit to the pre- and post-synaptic marker signals, and spots were considered co-localized if within 1 μm of each other. The spot counts per image were normalized to neurite volume, which was estimated from surface reconstruction of the NF-200 signal (neurons and soma) less the surface reconstruction of the DAPI signal (nucleus).

For multi-electrode array (MEA), 48-well MEA plates (Axion Biosystems; M768-tMEA-48B-5) were pre-coated in filter-sterilized 0.1% polyethyleneimine (Sigma-Aldrich; 181978-5G) diluted in borate buffer (Thermo Fisher; 28341) for 1 hour. After rinsing 4 times with sterile water, the plates were dried overnight in the biosafety cabinet. The following day, embryonic hippocampal and cortical cell suspensions were generated as described above and supplemented with mouse laminin (Thermo Fisher; 23017015; 1 μg/mL). A total of 50,000 cells/well in a volume between 5-10 μL were plated in the center of the well. After a 1-hour incubation at 37°C and 5% $CO_2$, 200 μL neuron culture media was added per well. The cells were maintained at 37°C and 5% $CO_2$ with a half media change every 3-4 days, and spontaneous activity recordings were taken every 7 days *in vitro* (DIV) using the Maestro Pro Multiwell Multielectrode Array and Impedance System (Axion Biosystems). Media changes were avoided on the day of recording. Before recording, the plate equilibrated in the MEA recording chamber for 5 minutes at 37°C and 5% $CO_2$. Data were collected for a 10-minute duration using the Axis Navigator software (Axion Biosystems; Version 2.0.2.5) with the Neural Real Time configuration for continuous spontaneous activity. A band-pass filter of 3,000 Hz (low-pass) to 200 Hz (high-pass) was applied with a variable threshold spike detector at ±6 standard deviations of the root mean squared of the background noise. A minimum spike rate of 5 spikes/minute was used to determine an active electrode, and a mature network was considered to be a well with at least 8 out of 16 active electrodes. Bursts were detected in mature networks using the inter-spike interval threshold with a maximum inter-spike interval of 100 ms and minimum number of 5 spikes. Network bursts were detected in mature networks with a maximum inter-spike interval of 100 ms, minimum number of 50 spikes, and minimum of 35% participating electrodes. A synchronicity window of 20 ms was applied. Mean firing rate (Hz) and burst rate (Hz) represent neural excitability while network burst rate (Hz) and network synchronicity (index value between 0 and 1) represent network synchronization.

## Neuron Isolation

Adult mice (3-10 months of age) were anesthetized with avertin (Sigma-Aldrich; T48402-25G) via intraperitoneal injection (250 mg/kg) and euthanized by decapitation; the brain was extracted, dissected to remove the olfactory bulbs and cerebellum, and processed into a single cell suspension using the adult brain dissociation kit for mouse and rat (Miltenyi Biotec; 130-107-677) with the gentleMACS octo dissociator with heaters (Miltenyi Biotec; 130-096-427). Up to $1\times10^7$ cells were processed using the neuron isolation kit (Miltenyi Biotec; 130-115-389) to separate neurons from non-neurons using the QuadroMACS separator (Miltenyi Biotec; 130-090-976).

## Diffusion-weighted imaging

On P120, mice were anesthetized with isoflurane then transcardially perfused with phosphate-buffered solution (PBS) followed by 4% paraformaldehyde (PFA) in 0.1 M PBS. Brains were extracted and post-fixed in 4% PFA. Imaged brains were placed in a custom-built holder immersed in Fluorinert (FC-3283, 3M, St. Paul, MN, USA) and imaged with a 4.7-T Agilent MRI system with a 3.5-cm diameter quadrature volume RF coil. Multi-slice, diffusion-weighted, spin echo images were used to acquire 10 non-diffusion-weighted images (b = 0 $s\bullet mm^{-2}$) and 75 diffusion-weighted images (25: b = 800 $s\bullet mm^{-2}$, 50: b = 2,000

s•mm$^{-2}$), using non-colinear diffusion-weighting directions. Other relevant imaging parameters include the following: TE/TR = 24.17/2000-ms, FOV = 30 × 30 mm$^2$, matrix = 192 × 192 reconstructed to 256 × 256 for an isotropic voxel size of 0.25-mm over two signal averages.

Raw data files were converted to NIfTI format. FSL was used to correct for eddy current artifacts. A diffusion-weighted imaging (DTI)-based mouse brain atlas was used as a template and to define ROIs, including the left and right hippocampus, amygdala, and corpus callosum.[45] Multishell diffusion data were fit with the Microstructure Diffusion Toolbox to models of neurite orientation dispersion and density imaging (NODDI) and ActiveAx.[46] An additional compartment of isotropic restriction was included to account for potential fixative effects as recommended.[47] Whole-brain voxel-wise differences between WT and SLC13A5 nTg animals for all MC-DWI indices were determined as previously described with tract-based spatial statistics.[48] An FA threshold of 0.2 was applied for the creation of the skeleton and permutation test results for multiple comparisons and threshold-free cluster enhancement (TFCE) was implemented with FSL's Randomize to compare the SLC13A5 nTg group to the WT group, with $p < 0.05$ as threshold for significance. Region-based differences between WT and SLC13A5 nTg animals were determined by calculating the indices of DWI in each diffusion model (FA, MD, NDI, ODI, IC, EC, and stat) for each ROI and comparing the values between WT and SLC13A5 nTg animals via an unpaired *t*-test (significance $p < 0.05$); statistically significant differences were then determined after controlling for multiple comparisons with the Benjamini-Hochberg procedure with the false discovery rate (FDR) set to 0.05.

## Electrophysiology

Extracellular recordings of field excitatory postsynaptic potentials (fEPSPs), long-term potentiation (LTP), and long-term depression (LTD) were conducted as previously described,[11] with the following modifications. Slice preparation solution contained the following: 124 mM NaCl, 1.25 mM $NaH_2PO_4$, 3 mM KCl, 25 mM $NaHCO_3$, 10 mM glucose, 1 mM sodium ascorbate, 3 mM kynurenic acid, 3.6 mM $MgSO_4$, and 0.8 mM $CaCl_2$. Recording artificial cerebrospinal fluid (aCSF) contained the following: 124 mM NaCl, 1.25 mM $NaH_2PO_4$, 3 mM KCl, 25 mM $NaHCO_3$, 15 mM glucose, 0.8 mM sodium ascorbate, 1.3 mM $MgSO_4$, and 2.5 mM $CaCl_2$. All solutions were buffered to pH 7.3 when saturated with carbogen and had a confirmed osmolality between 294-297 mOsm. Recordings were taken from coronal slices using fire-polished borosilicate glass recording pipettes filled with 1 M NaCl (3-5 MΩ) and Pt/Ir concentric bipolar stimulating electrodes. For LTD induction, 15 μM NMDA was perfused over the slice for 5 minutes at a rate of 3 mL/min. Potentiation and depression were defined as the mean fEPSP slope during the last 10 minutes of the recording divided by the average of the last 10 minutes of baseline immediately preceding induction of LTP or LTD.

## Synaptosome preparation

Crude synaptosomes (pre- and post-synaptic) were prepared from fresh or snap-frozen hippocampus and cortex using Syn-PER synaptic protein extraction reagent (Thermo Fisher; 87793) supplemented with protease inhibitor cocktail (Millipore; 11836170001) following manufacturer's instructions.

## Western blotting

Western blotting was conducted as previously described.[4,15,17] The following primary antibodies were used in this study: Neurexin 1 (Thermo Fisher; 18730; 1:1,000), Neuroligin 3 (Thermo Fisher; PA5-18849; 1:1,000), Rap2a (Thermo Fisher; 23298; 1:1,000); Ampa2/3/4 (Cell Signaling Technologies; 2460; 1:1,000), Synaptogyrin 1 (Abcam; ab113886; 1:1,000), Rab12 (Thermo Fisher; PA5-48179; 1:1,000), Psd-95 (Cell Signaling Technologies or Thermo Fisher; 3409 or MAI-045; 1:2,000 or 1:1,000), mGluR5 (Millipore; AB5675; 1:2,000), Syn-1 (Cell Signal Technologies; 5927S; 1:1,000), Homer1 (Synaptic Systems; 160-011; 1:1,000), Vglut2 (Synaptic Systems; 135-043; 1:1,000), and β-actin (Cell Signal Technologies; 3700 or 4967; 1:1,000 to 1:5,000).

Donkey anti-rabbit, donkey anti-goat, and goat anti-mouse IRDye 800CW, 680RD, and 680LT-conjugated secondary antibodies (LI-COR Biosciences; 925-32213, 925-32210, 926-68073, 926-68070, 926-68024) were used for infrared imaging on a LICOR Odyssey Infrared Imaging System (LI-COR Biosciences). The original uncropped Western blot images included in the manuscript can be found in Supplementary Figs. 6 and 7.

## Histology and immunostaining

Histology and immunostaining techniques were performed as described previously.[11,12,15,49] Klüver-Barrera staining on 10 μm paraffin-embedded slices was performed according to kit instructions (Electron Microscopy Sciences; 26681). Golgi staining was performed as previously described.[11] The following primary antibodies were used: myelin basic protein (Abcam; ab40390; 1:200), APC/CC-1 (Millipore; OP80; 1:50), Olig2 (Millipore; AB9610; 1:300), Slc13a5 (Santa Cruz Biotechnology; sc-293277; 1:100), and NeuN (Millipore; ABN91MI; 1:1,000).

Bright-field images were acquired using an upright Leica DM4000 B microscope with a 10x or 20x air objective using Image-Pro version 6.3. For high-magnification imaging of Golgi-stained sections, bright-field images were acquired using the Zeiss Axioplan2 upright microscope with a 100x oil objective using Köhler illumination and Q-imaging Retiga 2000r (1.92 MP 12 bit) monochrome camera (7.4 μm x 7.4 μm pixel resolution); z-stacks were collected every 1 μm for a total thickness of 40 μm using StereoInvesigator version 2021 software. All fluorescently labeled slides were imaged on a Nikon A1 inverted confocal microscope using NIS-Elements AR version 5.11.01 software with 405 nm (blue channel), 488 nm (green channel), 561 nm (red channel), and 640 nm (far red) laser wavelengths using the Galvano scan head. For Slc13a5/NeuN-stained slides, single z-slice images (1024 × 1024 pixels) were acquired using a 10x air objective (NA = 0.3; 1.24 μm/pixel) and 60x oil objective (NA = 1.4; 0.21 μm/pixel) at a pinhole size of 220.95 μm. For MBP/NeuN-stained slides, single z-slice images (1024 × 1024 pixels; 1.24 μm/pixel) were acquired using a 10x air objective (NA = 0.3) at a pinhole size of 166.03 μm. For CC-1/Olig2/NeuN-stained slides, single z-slice images (1024 × 1024 pixels; 0.63 μm/pixel) were acquired using a 20x air objective (NA = 0.75) at a pinhole size of 166.03 μm.

Golgi staining images were pre-processed in ImageJ (Version 1.52) by first inverting then using the Background Subtract tool 3 consecutive times with a pixel size of 100, 50, and 25. Images were saved as .tiff, imported into Imaris (Bitplane; Version 9.5), and converted into native .ims format. Secondary dendritic branches were semi-manually traced using the Autopath method of the Filament Tracer module with a diameter of 0.25 μm; automatic dendrite volume detection was enabled. To reduce computation time for spine detection, a mask was first created to eliminate signal distant from the reconstructed dendrites. Spines were identified with a minimum diameter of 0.25 μm, maximum length of 5 μm, and enabling for detection of branch spines. Dendrite spine density (in spines per 10 μm dendrite length) and spine volume ($\mu m^3$) were extracted for external analysis.

## Transmission Electron Microscopy

Following $CO_2$ euthanasia, the brain was extracted and left hippocampus micro-dissected in PBS. The tissue was subsequently fixed in 2.5% glutaraldehyde in 0.1 M phosphate buffer (PB) overnight at 4°C. The fixed samples were rinsed 5 × 5 minutes in PB and post-fixed in 1% osmium tetroxide, 1% potassium ferrocyanide in 0.1 M PB for 1 hour at room temperature, then rinsed in PB as before. Dehydration was performed in a graded EtOH series (35, 50, 70, 80, 90% for 10 minutes each step, 95% for 20 minutes, 100% for 2 × 10 minutes) at room temperature and 100% EtOH at 4°C overnight then transitioned in propylene oxide (PO) 2 × 7 minutes at room temperature. Fully dehydrated samples were infiltrated in increasing concentrations of PolyBed 812 (Polysciences Inc.) and PO mixtures. Embedding and polymerization took place in fresh PolyBed 812 for 24 hours at 60°C. The samples were sectioned on a Leica EM UC6 ultramicrotome at 100 nm, collected on formvar coated 2 × 1 mm slot Cu grids (EMS Hatfield, PA), and post-stained with uranyl acetate and lead citrate. The sectioned samples were viewed at 80 kV on a Philips CM120 transmission electron microscope equipped with AMT BioSprint12 digital camera (AMT Imaging Systems).

Images were analyzed on ImageJ (Version 1.52) using the GRatio plugin.[50] The G-ratio reported was calculated using the traced perimeter values (GRatioPerimeter). The axon diameter was calculated by dividing the traced axon perimeter by pi.

## Reverse transcription-quantitative PCR (RT-qPCR)

RNA extraction, cDNA synthesis, and RT-qPCR were performed as previously described.[8,10,14] The following primers and annealing temperatures not previously described were used: human SLC13A5 forward (5'-CTTTGTGGCCACCCTGCTATTC-3') and reverse (5'-AGCAAATTCGCCCCCTAGTA-3'), 55°C.

## Proteomics

Cortical and hippocampal tissues were lysed in 8 M urea buffer containing protease and phosphatase inhibitors (Thermo Fisher) followed by a minute of sonication. The lysate was reduced with 10 mM dithiothreitol (DTT) at 56°C for 30 minutes, then alkylated with 20 mM iodoacetamide at room temperature in the dark for an additional 15 minutes. Approximately 100 μg of protein was then digested with trypsin with a trypsin/protein ratio of 1:100 overnight at 37°C. Peptides were extracted

and dried (SpeedVac; Eppendorf), and concentrations of the peptide mixture were measured. Samples were lyophilized and stored at -80°C until further processing.

Dimethylated leucine (DiLeu) tags were synthesized as previously described.[51] DiLeu tags were activated in anhydrous DMF combined with DMTMM and NMM at 0.7× molar ratio and vortexed at room temperature for 45 minutes. After centrifugation, the supernatant was used immediately for peptide labeling. DiLeu labeling was performed by addition of labeling solution at a 20:1 tag to digested peptide ratio by weight and vortexed at room temperature for 2 hours. The labeling reactions were quenched by addition of hydroxylamine to a concentration of 0.25%, and the labeled peptide samples were dried in vacuo. The samples were combined and cleaned with SCX SpinTips (Protea Biosciences) and desalted with Omix C18 pipet tips (Agilent).

The liquid chromatography-tandem mass spectrometry (LC-MS/MS) detection system consisted of a nanoflow high-performance liquid chromatograph (HPLC) instrument (Dionex UltiMate 3000 UPLC system; Thermo Fisher) coupled to an Q Exactive HF Orbitrap mass spectrometer (Thermo Fisher) with a nanoelectrospray ion source (Thermo Fisher). In brief, 0.5 µg of peptide mixture dissolved in buffer A (0.1% formic acid (FA)) was loaded onto a 75 µm x 15 cm fabricated column filled with 1.7 µm Bridged Ethylene Hybrid packing materials (130 Å; Waters) over a 126-min linear gradient of 3-45% Mobile Phase B (buffer A, 0.1% FA in water; buffer B, 0.1% FA in ACN) with a flow rate of 300 nl/min. The MS analysis was performed in a data-dependent manner using an Orbitrap mass analyzer. For a full mass spectrometry survey scan, the target value was $1 \times 10^5$, and the scan ranged from 300 to 1,500 *m/z* at a resolution of 60,000, with a maximum injection time of 100 ms. For the MS2 scan, up to 15 of the most intense precursor ions from a survey scan were selected for MS/MS and detected by the Orbitrap at a mass resolution of 15,000 at *m/z* 400. Only precursor ions with charge states of 2-6 were selected for fragmentation by higher-energy collision dissociation with a normalized collision energy of 30%. The automatic gain control for MS/MS was set to 8e3, with maximum ion injection times of 100 ms. Dynamic exclusion time was 45 seconds, and the window for isolating the precursors was 1.4 *m/z*.

Protein and peptide identification and quantification were conducted through MaxQuant version 1.5.3.8.[52] Raw files were searched against the Uniprot mouse reviewed database (August, 2019) using the integrated Andromeda search engine with FDR < 1% at the peptide and protein level. Trypsin was selected as the enzyme with at most two missed cleavages. A reverse database for the decoy search was generated automatically in MaxQuant. Enzyme specificity was set to 'Trypsin', with a minimum number of seven amino acids were required for peptide identification. Static modifications included carbamidomethylation of cysteine residues (+57.02146 Da) and DiLeu labeling on N-terminus and lysine residues (+145.12801 Da). Dynamic modifications included oxidation of methionine residues (+15.99492 Da) and deamidation of asparagine and glutamine residues (+0.98402 Da). The first search mass tolerance was 20 ppm, and the main search peptide tolerance was 4.5 ppm. The false discovery rates of the peptide-spectrum matches and proteins were set to less than 1%. Quantitation was performed using Perseus software.[53] Briefly, the raw reporter ion intensity in each DiLeu channel was corrected for isotope impurities[51] and normalized for mixing differences by equalizing the total signal in each channel. In cases where no signal was detected in a channel, the missing value was assigned with the noise level

of the original spectrum (noise-band capping of missing channels), and the resultant intensity was not corrected for impurities or normalized for uneven mixing.

## Stoichiometry of protein acetylation

Cortical and hippocampal tissue was prepared and analyzed as previously described.[18] Acetyl stoichiometry values are reported as a range from 0-1 representing 0%-100% of a detected lysine site being endogenously acetylated, respectively. Changes in acetyl stoichiometry values ($\Delta$ acetyl stoichiometry) are consistently reported as the nTg value less the WT value. Pathway analysis and network plot construction was conducted using the R package enrichplot with an overrepresentation analysis (ORA) using the *Mus musculus* organism database.[54] Relevant parameters included a minimum and a maximum number of genes for a category of 5 and 2,000, respectively, with the Benjamini-Hochberg method for multiple test adjustment to a FDR of 0.05.

## Statistical analysis

Data analysis was performed using GraphPad Prism version 9.0.1. Data are expressed as mean ± SD unless otherwise specified. Comparison of the means was performed using an unpaired *t*-test for 2 groups and ordinary one-way or two-way ANOVA for ≥3 groups followed by either Tukey-Kramer (comparison between all groups) or Dunnett's (comparison to one control group) multiple comparisons test. If no sex differences were found via ANOVA testing, data were combined for ease of visualization. The details of each statistical test are described in the figure legends. Grubb's test was used to remove outliers, which are determined at $p < 0.05$. Differences in the mean were declared statistically significant if $p < 0.05$, and the following statistical significance indicators are used throughout the article: $*p < 0.05$; $**p < 0.005$; $***p < 0.0005$.

## Data availability

The proteomics data that support the findings of this study have been deposited to the ProteomeXchange Consortium (ID number PXD026624). The acetyl-proteomics data that support the findings of this study have been deposited to the ProteomeXchange Consortium (ID number PXD025424) and the MassIVE partner repository (ID number MSV000087209). The authors declare that all other data supporting the findings of this study are available within the paper and its Supplementary Data/Tables.

# Results

## SLC13A5 nTg mice exhibit an autistic-like phenotype with jumping stereotypy

To evaluate our hypothesis that increased citrate flux into the cytosol can cause an autistic-like phenotype, we generated transgenic C57BL/6J mice that specifically overexpress human SLC13A5 in forebrain neurons, henceforth referred to as the neuron transgenic (nTg), using the same expression system as the previously reported AT-1 nTg model.[11] To ensure our transgenic system was working as expected, we performed RT-qPCR on cDNA from isolated adult neurons using primers specific for human SLC13A5; as expected, we observed a PCR product only with SLC13A5 nTg cDNA and not in WT controls (*Figure 1A*). Additionally, immunofluorescence staining of hippocampal brain slices revealed a robust increase in SLC13A5 protein in the SLC13A5 nTg slices that co-localized with the neuronal marker NeuN (*Figure 1B*). These data support the successful generation of a transgenic mouse line that exhibits forebrain neuron-specific overexpression of SLC13A5.

Upon generation of the transgenic mouse line, it became apparent that the SLC13A5 nTg mice exhibited repetitive bouts of repetitive jumping behavior in their home cage seen both during the day and night cycle while their WT littermates did not (*Supplementary Movie 1*). This behavior was formally quantified with the mice undisturbed in their home cage by counting the number of jumps in a 50-second time period (*Figure 2A*). Interestingly, in an open field (OF) assay, the SLC13A5 nTg mice did not exhibit a change in vertical activity compared to WT controls, suggesting this jumping stereotypy was suppressed in an unfamiliar environment (*Figure 2B*). The OF assay also revealed a decrease in the overall total distance traveled, distance traveled in the center of the arena, and ambulatory time (*Figure 2B*). In a light-dark (LD) assay, the SLC13A5 nTg mice entered the light side less frequently but did not spend significantly more time on either side compared to WT controls (*Figure 2C*). In sum, these data show that SLC13A5 nTg mice exhibit repetitive jumping behavior while in their home cage but have reduced ambulatory activity in a novel environment.

We also performed several behavioral assays to gauge both learning and memory formation as well as autistic-like features like we did in the AT-1 nTg model.[11] In a marble burying (MB) assay, the SLC13A5 nTg mice buried less marbles compared to WT controls (*Figure 2D*), which was also observed in the AT-1 nTg mice.[11] Furthermore, the SLC13A5 nTg mice spent more time investigating both novel and familiar objects in a novel object recognition (NOR) paradigm; however, they did not display a change in the percentage of time investigating the novel object (*Figure 2E*). In a fear conditioning (FC) paradigm, the SLC13A5 nTg mice compared to WT controls displayed reduced freezing behavior after conditioning (day 2), but not during training (day 1), revealing reduced learning and memory formation in the transgenic mice (*Figure 2F*). Moreover, the SLC13A5 nTg mice preferred interacting with a mouse over an empty cup like WT mice in a social interaction (SI) assay, but when presented with a familiar or novel mouse, the SLC13A5 nTg mice did not significantly distinguish the two like WT controls (*Figure 2G*). Overall, the behavioral abnormalities observed in the SLC13A5 nTg mice are similar to the AT-1 nTg in the MB, FC, and SI assays,[11] leading us to conclude the SLC13A5 nTg mouse exhibits an autistic-like phenotype.

## White matter integrity is disrupted in SLC13A5 nTg mice

Changes in white matter microstructure are commonly observed in individuals with ASD.[26,27] Therefore, we desired to assess the white matter integrity of our autistic-like SLC13A5 nTg model by performing *ex vivo* diffusion-weighted imaging (DWI) using both region of interest (ROI) and tract-based spatial

statistics (TBSS) analyses with three different diffusion models: diffusion tensor imaging (DTI), neurite orientation dispersion and density imaging (NODDI), and ActiveAx. We selected the right/left hippocampus and right/left amygdala ROIs based upon the behavioral aberrations observed and included the right/left corpus callosum as comparison ROIs where we did not expect to observe differences. The DTI analysis revealed a decrease in fractional anisotropy (FA) within the left hippocampus and right/left amygdala (*Figure 3A*); likewise, our TBSS analysis revealed multiple clusters of voxels with decreased FA (*Figure 3B*). We also observed an increase in DTI mean diffusivity (MD) in the TBSS analysis, but no changes in the ROI analysis survived corrections for multiple comparisons (*Figure 3A-B*). NODDI modeling did not reveal any changes in WT versus SLC13A5 nTg mice (*Supplementary Figure 1*). ActiveAx revealed an increase in the "extra-neuronal/extracellular" EC parameter in the left hippocampus as well as a decrease in the "intra-neuronal" IC parameter in the right/left amygdala and increase in the right corpus callosum (*Figure 3A*). No changes in the ActiveAx stat parameter were observed (*Supplementary Figure 1*). Taken together, these results suggest disruptions in the integrity of white matter that can be from a number of causes, including changes within the axonal tracts or myelin structure or composition.[28] To address potential changes in myelination, we first performed basic histologic assessment of our SLC13A5 nTg mice and found no obvious anatomic differences (*Supplementary Figure 2A*). Additionally, we performed immunofluorescence staining for oligodendrocytes, which also did not reveal any changes from WT mice (*Supplementary Figure 2B-C*). Finally, we processed the left hippocampus from WT and SLC13A5 nTg mice for transmission electron microscopy for high-resolution imaging to visualize myelinated axons. We specifically examined for differences in myelination of the perforant path axons within the dentate gyrus stratum moleculare. There was a trend for smaller axon diameter in the SLC13A5 nTg, but this did not achieve statistical significance (*Figure 3C*). However, by plotting the G-ratio versus axon diameter, we observed significantly more small diameter axons with higher G-ratios in the SLC13A5 nTg mice, supporting reduced thickness of myelin in the transgenic mice (*Figure 3C*). Overall, these data reveal widespread disruptions in white matter integrity in the SLC13A5 nTg mice that is potentially a result of aberrant myelination.

## SLC13A5 nTg mice have abnormal synaptic plasticity and spontaneous electrical activity

In addition to alterations in white matter microstructure, we assessed both synaptic structure and function in our SLC13A5 nTg mice, as the AT-1 nTg model displayed changes in synaptic density and biochemical composition.[11] We first performed hippocampal brain slice electrophysiology to assess synaptic plasticity, specifically probing the Schaffer collateral synapse from CA3 onto CA1 pyramidal neurons. We did not observe any difference in long-term potentiation (LTP) (*Figure 3D*), but there was a robust increase in long-term depression (LTD) in the SLC13A5 nTg mice compared to WT controls (*Figure 3E*). Furthermore, we used the Golgi staining method to visualize neuron morphology *in vivo*, like for the AT-1 nTg, to evaluate for potential explanations of enhanced LTD in the SLC13A5 nTg mice. We did not observe obvious changes in neuron morphology, namely the density of dendritic branching, at low magnification (*Supplementary Figure 3*). We then took high magnification images of the CA1 pyramidal

neurons to quantify dendritic spine density and morphology of their apical dendrites. We did not observe differences in dendritic spine density, but there was an increase in spine volume observed in the SLC13A5 nTg mice compared to WT controls (*Figure 3F*). Finally, we evaluated protein expression levels in crude synaptosomes focusing on the proteins that significantly increased in the AT-1 nTg model.[11] To our surprise, we found minimal differences in both the cortex and hippocampus in male and female SLC13A5 nTg mice versus WT controls (*Supplementary Figure 4*). Therefore, *in vivo*, our SLC13A5 nTg mice exhibited altered Schaffer collateral-to-CA1 synaptic plasticity with a change in CA1 pyramidal neuron apical dendritic spine morphology. We also uncovered several phenotypic differences from the AT-1 nTg model.

To better characterize neuron morphology and synapse formation, we cultured primary embryonic neurons from WT and SLC13A5 nTg littermates *in vitro*, performing parallel experiments on both cortical and hippocampal neurons. We expected to see similar changes in neuron morphology like was observed for the AT-1 nTg model, namely increased dendritic branching and spine formation.[11] After 15 days *in vitro* (DIV), we were surprised to find that SLC13A5 nTg cortical neurons did not exhibit changes from WT in dendritic branching, dendritic spine density, or spine morphology (*Figure 4A*). In addition to quantifying dendritic spine density, we also assessed spontaneous synapse formation 15 DIV by immunofluorescence staining for the pre-synaptic marker Syn-1 and post-synaptic marker Psd-95. When normalized to neurite volume, we observed a decrease in puncta density for both Syn-1 and Psd-95 as well as a reduction in co-localization between the puncta, suggesting reduced synaptic density in the SLC13A5 nTg cortical neurons compared to WT (*Figure 2B*). Finally, to assess the activity of our neurons, we plated them on multielectrode arrays and monitored their spontaneous activity every 7 days for a total of 28 DIV. We monitored the spontaneous activity of our neurons by examining the number of active electrodes, mean firing rate, and burst frequency; the network activity, implying functional neuron-to-neuron communication, was quantified by network burst frequency and synchronicity index. It is important to note that the activity parameters (mean firing rate, burst frequency, network burst frequency, and network synchronicity) required a network to have at least 8 out of 16 active electrodes. At every time point, the SLC13A5 nTg cortical neurons had significantly more active electrodes compared to WT, and the mean firing rate was significantly higher at 14 and 21 DIV (*Figure 4C*). Note that activity parameter comparisons could not be made at 7 DIV since there were no WT networks that exhibited at least 8 active electrodes. Moreover, the SLC13A5 nTg cortical networks exhibited a higher burst frequency at 14 and 21 DIV; higher network burst frequency at 14 and 28 DIV; and higher synchronicity index at 14 DIV (*Figure 4C*). Our hippocampal primary neurons exhibited similar findings to the cortical neurons in morphology (*Figure 5A*), but the hippocampal neurons had almost no changes in synaptic density or spontaneous electrical activity (*Figure 5B-C*). Overall, our data show the SLC13A5 nTg mice exhibit changes in synaptic plasticity and dendritic spine morphology *in vivo* as well as synaptic density and spontaneous electrical activity *in vitro*, with notable differences from the previously characterized AT-1 nTg autistic-like model and between cortical and hippocampal-derived neurons.

## SLC13A5 overexpression results in differential proteomic and acetyl-proteomic adaptations

To evaluate the molecular underpinning of the SLC13A5 nTg phenotype, we conducted quantitative proteomics on both hippocampal and cortical tissue. The total numbers of proteins detected were 1,592 and 1,580 in the hippocampus and cortex, respectively; of these proteins detected, 607 and 107 in the hippocampus and cortex, respectively, exhibited an expression level that was significant different ($p < 0.05$) from WT controls (*Figure 6A*). Interestingly, the overall fold change in the detected proteome was significantly different between the hippocampus and cortex (*Figure 6B*), and only 37 of the significantly changed proteins overlapped between the two tissue types (*Figure 6C*). KEGG pathway analysis of the proteins that exhibited statistically significant changes from WT resulted in multiple overlapping categories related to glucose metabolism, including oxidative phosphorylation, carbon metabolism, and citrate cycle (TCA cycle) (*Figure 6D*). These same proteins were also analyzed in the gene ontology (GO) cellular component function database to construct a gene-network plot, which revealed several categories that directly apply to the SLC13A5 nTg phenotype including myelin sheath, synaptic vesicle, and neuron-to-neuron synapse (*Figure 6E*).

To complement the proteome, we also characterized the acetyl-proteome due to hypothesized changes in protein acetylation from increased transport of citrate into the cytosol. Acetylation can dramatically impact protein function independent of protein expression level,[29] which may play an important role in the SLC13A5 nTg phenotype. As such, we performed subcellular fractionation (cytoplasmic, nuclear/membrane, and chromatin-associated) on hippocampal and cortical tissue in order to increase our detection resolution.[30] In all fractions combined, we detected 2,506 and 3,886 protein acetylation sites (hereafter referred to as acetylpeptides) in the hippocampus and cortex, respectively. The following number of acetylpeptides exhibited a statistically significant change in acetylation stoichiometry from WT controls ($p < 0.05$): cytoplasmic, 26 in the hippocampus and 39 in the cortex; nuclear/membrane, 18 in the hippocampus and 45 in the cortex; chromatin-associated, 52 in the hippocampus and 27 in the cortex (*Figure 7A-B*). Three acetylpeptides were detected in multiple fractions (*Figure 7B*). When the acetylpeptides from all 3 fractions were combined, 9 of these overlapped between the hippocampus and cortex, with many exhibiting opposite changes in acetyl stoichiometry (*Figure 7C*). To assess the biological impact of these acetylation changes, a KEGG pathway analysis was conducted on the proteins harboring the significantly changed acetylation sites in both the hippocampus and cortex. Again, there was a predominance of glucose metabolism-related categories including carbon metabolism and citrate cycle (TCA cycle) (*Figure 7D*). Finally, the GO cellular component gene-network plots were strikingly similar between the hippocampus and cortex despite the minimal overlap between the acetylation sites, containing several relevant categories such as myelin sheath, neuron-to-neuron synapse, and postsynaptic density (*Figure 7E*). Similar to the proteomic analysis, the SLC13A5 nTg acetyl-proteome revealed differential adaptations between the hippocampus and cortex with changes consistent with the autistic-like phenotype. Finally, both the proteome and acetyl-proteome might also highlight a compensatory response from glia.

Global profiling of both the proteome and acetyl-proteome in the SLC13A5 nTg mouse allowed us to assess the overlap between the significantly affected proteins in both analyses. There was a larger overlap between the proteome and acetyl-proteome in the hippocampus versus the cortex with 29 and 3 commonly shared proteins, respectively (*Figure 8A*). To better illustrate this, we constructed a manual cluster plot using the proteins found within the single overlapping GO cellular component myelin sheath category between the proteome and acetyl-proteome (see gene-network plots in *Figure 6E* and *7E*). This plot demonstrates that a majority of the proteins were regulated at either the level of the proteome or the acetyl-proteome, and a handful of proteins exhibited complex changes both in the protein expression level and acetylation stoichiometry, sometimes in multiple lysine sites (*Figure 8B*). It is interesting to note that, proportionally, changes in the hippocampus were driven more by changes in protein abundance, whereas changes in the cortex were driven more by changes in acetylation. Finally, we sorted the proteins in both the acetyl-proteome and proteome analyses by their subcellular localization, revealing that approximately 40% of the proteins impacted by SLC13A5 overexpression flux through the secretory pathway (i.e. localize to the endoplasmic reticulum, Golgi apparatus, membrane, or are secreted; *Supplementary Figure 5A*). GO cellular component gene-network plots using these secretory pathway-related proteins revealed categories similar to before, such as myelin sheath, neuron-to-neuron synapse, and postsynaptic density, emphasizing the importance of this subset of proteins in the SLC13A5 nTg phenotype (*Supplementary Figure 5B*). Taken together, the SLC13A5 nTg hippocampus and cortex displayed differential adaptations in the proteome and acetyl-proteome, with changes in metabolism being a potentially important mechanism underlying the mouse phenotype.

# Discussion

Here we reported that overexpression of SLC13A5 restricted to forebrain neurons results in an autistic-like phenotype with jumping stereotypy. The mice displayed disruptions in white matter integrity as well as aberrant synaptic structure and function both *in vivo* and *in vitro*. Finally, the proteome and acetyl-proteome uniquely adapted to SLC13A5 overexpression within the hippocampus and cortex, which implicated the potential importance of metabolic changes in the phenotype observed.

Prior study of the autistic-like AT-1 nTg mouse led us to the conclusion that increased flux of acetyl-CoA from the cytosol to the ER may be a mechanistic driver of ASD.[11] This is supported by the observation that gene duplication events in *AT-1/SLC33A1*, *SLC25A1*, *SLC13A5*, and *ACLY* are all associated with ASD.[24] Importantly, AT-1 overexpressing neurons exhibited cellular adaptations to maintain the cytosolic-to-ER flux of acetyl-CoA by upregulation of SLC25A1 and ACLY, which act in concert to deliver additional citrate to the cytosol for conversion to acetyl-CoA.[11] The results presented here affirm that SLC13A5 overexpression also results in an autistic-like phenotype, likely from increased citrate/acetyl-CoA availability in the cytosol and flux of acetyl-CoA into the ER. Indeed, approximately 40% of the proteins affected in the SLC13A5 nTg acetyl-proteome and proteome localized to the secretory pathway and were relevant to the phenotypic features of the mouse model. Targeting the ER acetylation machinery, such as by inhibition of the $N^{\varepsilon}$-lysine acetyltransferases ATase1 and ATase2,[2,10,12,16] is an

active area of investigation to assess the direct contribution of changes in ER-based acetylation in the development of the autistic-like phenotype in the SLC13A5 nTg mouse.

Alterations in membrane physiology or organelle adaptations outside of the ER as a result of SLC13A5 overexpression are also likely to play a role in the phenotype that we observed. First, SLC13A5 functions as a sodium co-transporter, carrying in 4 $Na^+$ for every dicarboxylate or tricarboxylate molecule imported into the cell,[25] which results in membrane depolarization. This impact on membrane potential may have substantial implications for neuron physiology – especially when SLC13A5 is expressed at high levels – that likely triggers changes within the neuron to account for this continuous source of membrane depolarization. Our proteomic dataset supports this as we saw changes in expression levels of $Na^+/K^+$-ATPase subunits, namely Atp1a1, Atp1a2, Atp1a3, Atp1b1, and Atp1b2, as well as other proteins involved in membrane excitability including Slc8a2, Scn2a, and Scn2b. It is also important to point out that human SLC13A5 is low-affinity/high-capacity transporter for citrate, which is in contrast to mouse Slc13a5 that is a high-affinity/low-capacity transporter[31,32]; this results in significantly more citrate import into the cell over the same amount of time for the human transporter compared to the mouse transporter. Furthermore, within the neuron, citrate participates in the synthesis of the neurotransmitters acetylcholine, glutamate, and GABA,[32] and altered availability of citrate within the cytosol may impact one or all of these neurotransmitter systems. Interestingly, we did see expression level changes in several genes related to neurotransmission including the glutamate receptors Grm2, Grm5, and Grin2a; GABA receptor subunits Gabra1 and Gabbr1; the diazepam binding inhibitor Dbi; and vesicle-associated proteins Snap25 and Sygr3.

The critical role of human SLC13A5 in neuron physiology is emphasized by loss-of-function mutations associated with early infantile epileptic encephalopathy-25 (EIEE25),[33,34] which may in part be due to imbalances in GABA synthesis. Likewise, deletion of mouse Slc13a5 results in a propensity for epileptic seizures, and quantitative proteomic analysis revealed disruptions in GABA and serotonin synthesis as well as adaptations in oxidative phosphorylation and lipid metabolism.[35] Our proteome and acetyl-proteome analyses strongly suggest changes in glucose metabolism within the SLC13A5-overexpressing neurons, which is not surprising given the central role of citrate and acetyl-CoA in cellular energetics as well as the aforementioned mouse Slc13a5 knockout study. We propose that the neuron is likely accommodating for membrane depolarization by excessive $Na^+$/citrate co-transport, which would require additional ATP to run the $Na^+/K^+$-ATPase. It would not be surprising if the SLC13A5 nTg mouse exhibits increased capacity for oxidative phosphorylation to generate additional ATP. There may be uncharacterized adaptations in the SLC13A5 nTg mitochondria that are a result of altered histone acetylation and methylation signatures, which was observed in the AT-1 nTg model.[11]

Dissecting the phenotype of the SLC13A5 nTg mouse revealed unexpected but intriguing differences from the AT-1 nTg mouse. First, the SLC13A5 nTg mice exhibited a jumping stereotypy while in their home cage, which was not observed in the AT-1 nTg model but is a feature of other rodent ASD models including the C58/J inbred mouse strain and *Jakmip1* knockout mouse.[11,36,37] Second, unlike the AT-1 nTg, the SLC13A5 nTg mice displayed reduced locomotion as demonstrated by the OF and LD assays, but oddly this behavior was not observed in the NOR or FC assays as demonstrated by overall increased time exploring objects and similar freezing behavior on the training day, respectively. It appears that the

SLC13A5 nTg behavior is variable depending on the context, such as repetitively jumping when undisturbed in the home cage versus overly engaged in exploration during the NOR assay. It is also important to mention that the cognitive deficits we observed in the FC and SI assays are in contrast to improved cognitive function observed in a mouse Slc13a5 knockout model,[38] suggesting the importance of balanced Slc13a5 function in learning and memory function. We have not excluded the possibility that the unusual behavior observed in the SLC13A5 nTg model could fit into other categories of neurodevelopmental diseases, such as Attention Deficit/Hyperactivity Disorder (ADHD), which has considerable overlap with ASD.[39-41] Further behavioral testing, such as motor impulsiveness, could better categorize the behavioral phenotype of the SLC13A5 nTg mouse.[42] Finally, SLC13A5 nTg mice did not exhibit changes in hippocampal LTP, dendritic branching and spine formation, or synaptosome protein expression like the AT-1 nTg model.[11] It is important to point out that we used crude synaptosomes unlike in the AT-1 nTg study where purified post-synaptic densities were used for Western blotting; therefore, our synaptosomes may have not been pure enough to detect subtle changes in protein expression. The SLC13A5 nTg mice did, however, have increased dendritic spine volume *in vivo*. Therefore, even with the similar behavioral abnormalities between the two autistic-like models, the underlying cellular and molecular changes are rather distinct. This likely highlights the importance of other mechanisms beyond ER-based $N^{\varepsilon}$-lysine acetylation in the SLC13A5 nTg mice that are contributing to the development of the phenotype, such as the differential effect of the AT-1 and SLC13A5 manipulations on the cytosolic pools of citrate and acetyl-CoA, and consequent functional responses.

Via *ex vivo* diffusion-weighted imaging and transmission electron microscopy, we found disrupted white matter integrity in the SLC13A5 nTg mice with evident changes in myelination in the hippocampus. What remains to be elucidated is whether these changes are due to an exclusive problem in the neurons or a defect in neuron-to-oligodendrocyte communication. Our proteome and acetyl-proteome suggest that SLC13A5 overexpression results in widespread changes in both protein expression level and acetylation status of multiple genes involved in myelination, but the specific cell type exhibiting those changes was not resolved. Alterations in neuronal secretory proteins or metabolites like *N*-acetylaspartate could impact oligodendrocyte function at multiple points during neurodevelopment,[43,44] and more detailed exploration could reveal a new function of ER-based $N^{\varepsilon}$-lysine acetylation in this neuron-to-glia communication.

Both our primary neuron and proteome/acetyl-proteome analyses revealed unique adaptations in the hippocampus versus cortex to SLC13A5 overexpression. This was evident by changes observed in synaptic density and spontaneous electrical activity in primary neurons derived from the cortex but not hippocampus, as well as different sets of changes in protein expression and acetyl stoichiometry between the cortex and hippocampus. It is important to note that our hippocampal primary neurons are more active with networks maturing more quickly compared to our cortical neurons, potentially from culture conditions that were originally optimized for hippocampal primary neuron cultures. Additionally, the population of neuron subtypes within the hippocampal and cortical cultures may be relevant, especially if membrane potential and neurotransmitter synthesis are impacted by SLC13A5 overexpression.

In conclusion, by overexpressing SLC13A5 in mouse forebrain neurons, we have reinforced the conclusion that aberrant citrate/acetyl-CoA flux within the neuron is a mechanistic driver of an autistic-like phenotype, resulting in disrupted white matter integrity, changes in synaptic structure and plasticity, and widespread adaptations in the proteome and acetyl-proteome. The metabolic versus ER-based $N^{\varepsilon}$-lysine acetylation contributions to the SLC13A5 nTg phenotype remain to be elucidated.


# Acknowledgements

We would like to thank Kathy Krentz at the Genome Editing & Animal Models Core of UW-Madison for the generation of the SLC25A1 transgenic mice; Heather Mitchell at the UW-Madison Waisman Behavior Testing Service for conducting mouse behavior testing; and B. Sheehan and Y. Peng for technical assistance.

# Funding

This research was supported by National Institutes of Health (NIH) R01 NS094154, R01 GM065386, F30 AG066329, RF1 AG052324, U01 CA231081, R01 DK071801, and P41 GM108538 and a core grant to the Waisman Center from NICHD-U54 HD090256. M.J.R. was supported in part by the Wisconsin Distinguished Graduate Fellowship. I.A.D. was supported by T32 AG000213. J.J.Y. was supported by the Clinical and Translational Science Award (CTSA) program, through the NIH National Center for Advancing Translational Sciences (NCATS), grant UL1TR002373. Additional imaging support was provided by the University of Wisconsin Carbone Cancer Center Support Grant P30CA014520 and Waisman Core Grant P30 HD003352-45 and U54 AI117924-03. The content is solely the responsibility of the authors and does not necessarily represent the official views of the NIH.


# Competing interests

The authors declare the following competing interests: J.M.D. is a co-founder of Galilei BioScience Inc and a consultant for Evrys Bio. Remaining authors have no competing interests to disclose.

# Supplementary material

Supplementary material is available at *Brain Communications* online.

# References


1. Ko MH, Puglielli L. Two endoplasmic reticulum (ER)/ER Golgi intermediate compartment-based lysine acetyltransferases post-translationally regulate BACE1 levels. *J Biol Chem.* 2009;284(4):2482-2492.
2. Duran-Aniotz C, Cornejo VH, Hetz C. Targeting endoplasmic reticulum acetylation to restore proteostasis in Alzheimer's disease. *Brain.* 2016;139(Pt 3):650-652.
3. Pehar M, Jonas MC, Hare TM, Puglielli L. SLC33A1/AT-1 protein regulates the induction of autophagy downstream of IRE1/XBP1 pathway. *J Biol Chem.* 2012;287(35):29921-29930.
4. Costantini C, Ko MH, Jonas MC, Puglielli L. A reversible form of lysine acetylation in the ER and Golgi lumen controls the molecular stabilization of BACE1. *Biochem J.* 2007;407(3):383-395.
5. Pehar M, Lehnus M, Karst A, Puglielli L. Proteomic assessment shows that many endoplasmic reticulum (ER)-resident proteins are targeted by N(epsilon)-lysine acetylation in the lumen of the organelle and predicts broad biological impact. *J Biol Chem.* 2012;287(27):22436-22440.
6. Mak AB, Pehar M, Nixon AM, et al. Post-translational regulation of CD133 by ATase1/ATase2-mediated lysine acetylation. *J Mol Biol.* 2014;426(11):2175-2182.
7. Farrugia MA, Puglielli L. Nepsilon-lysine acetylation in the endoplasmic reticulum - a novel cellular mechanism that regulates proteostasis and autophagy. *J Cell Sci.* 2018;131(22).

8. Peng Y, Puglielli L. N-lysine acetylation in the lumen of the endoplasmic reticulum: A way to regulate autophagy and maintain protein homeostasis in the secretory pathway. *Autophagy.* 2016;12(6):1051-1052.
9. Pehar M, Puglielli L. Lysine acetylation in the lumen of the ER: a novel and essential function under the control of the UPR. *Biochim Biophys Acta.* 2013;1833(3):686-697.
10. Peng Y, Shapiro SL, Banduseela VC, et al. Increased transport of acetyl-CoA into the endoplasmic reticulum causes a progeria-like phenotype. *Aging Cell.* 2018;17(5):e12820.
11. Hullinger R, Li M, Wang J, et al. Increased expression of AT-1/SLC33A1 causes an autistic-like phenotype in mice by affecting dendritic branching and spine formation. *J Exp Med.* 2016;213(7):1267-1284.
12. Peng Y, Kim MJ, Hullinger R, et al. Improved proteostasis in the secretory pathway rescues Alzheimer's disease in the mouse. *Brain.* 2016;139(Pt 3):937-952.
13. Ding Y, Dellisanti CD, Ko MH, Czajkowski C, Puglielli L. The endoplasmic reticulum-based acetyltransferases, ATase1 and ATase2, associate with the oligosaccharyltransferase to acetylate correctly folded polypeptides. *J Biol Chem.* 2014;289(46):32044-32055.
14. Rigby MJ, Ding Y, Farrugia MA, et al. The endoplasmic reticulum acetyltransferases ATase1/NAT8B and ATase2/NAT8 are differentially regulated to adjust engagement of the secretory pathway. *J Neurochem.* 2020;154(4):404-423.
15. Peng Y, Li M, Clarkson BD, et al. Deficient import of acetyl-CoA into the ER lumen causes neurodegeneration and propensity to infections, inflammation, and cancer. *J Neurosci.* 2014;34(20):6772-6789.

16. Ding Y, Ko MH, Pehar M, et al. Biochemical inhibition of the acetyltransferases ATase1 and ATase2 reduces beta-secretase (BACE1) levels and Abeta generation. *J Biol Chem.* 2012;287(11):8424-8433.
17. Jonas MC, Pehar M, Puglielli L. AT-1 is the ER membrane acetyl-CoA transporter and is essential for cell viability. *J Cell Sci.* 2010;123(Pt 19):3378-3388.
18. Dieterich IA, Lawton AJ, Peng Y, et al. Acetyl-CoA flux regulates the proteome and acetyl-proteome to maintain intracellular metabolic crosstalk. *Nat Commun.* 2019;10(1):3929.
19. Dieterich IA, Cui Y, Braun MM, et al. Acetyl-CoA flux from the cytosol to the ER regulates engagement and quality of the secretory pathway. *Sci Rep.* 2021;11(1):2013.
20. Rigby MJL, A. J.; Kaur, G.; Banduseela, V. C.; Kamm, W. E.; Lakkaraju, A.; Denu, J. M.; Puglielli, L. Endoplasmic reticulum acetyltransferases Atase1 and Atase2 differentially regulate reticulophagy, macroautophagy and cellular acetyl-CoA metabolism. *Comms Bio.* 2021.
21. Sheehan BK, Orefice, N.S., Peng, Y., Shapiro, S.L., Puglielli, L. ATG9A Regulates Proteostasis Through Reticulophagy Receptors FAM134B and SEC62 and Folding Chaperones CALR and HSPB1. *ISCIENCE.* 2021.
22. Huppke P, Brendel C, Korenke GC, et al. Molecular and biochemical characterization of a unique mutation in CCS, the human copper chaperone to superoxide dismutase. *Hum Mutat.* 2012;33(8):1207-1215.
23. Lin PF, Li JW, Liu QJ, et al. A Missense Mutation in SLC33A1, which Encodes the Acetyl-CoA Transporter, Causes Autosomal-Dominant Spastic Paraplegia (SPG42). *American Journal of Human Genetics.* 2008;83(6):752-759.

24. Sanders SJ, Ercan-Sencicek AG, Hus V, et al. Multiple recurrent de novo CNVs, including duplications of the 7q11.23 Williams syndrome region, are strongly associated with autism. *Neuron.* 2011;70(5):863-885.
25. Inoue K, Zhuang L, Maddox DM, Smith SB, Ganapathy V. Structure, function, and expression pattern of a novel sodium-coupled citrate transporter (NaCT) cloned from mammalian brain. *J Biol Chem.* 2002;277(42):39469-39476.
26. Hiremath CS, Sagar KJV, Yamini BK, et al. Emerging behavioral and neuroimaging biomarkers for early and accurate characterization of autism spectrum disorders: a systematic review. *Transl Psychiatry.* 2021;11(1):42.
27. Li D, Karnath HO, Xu X. Candidate Biomarkers in Children with Autism Spectrum Disorder: A Review of MRI Studies. *Neurosci Bull.* 2017;33(2):219-237.
28. Alexander AL, Lee JE, Lazar M, Field AS. Diffusion tensor imaging of the brain. *Neurotherapeutics.* 2007;4(3):316-329.
29. Verdin E, Ott M. 50 years of protein acetylation: from gene regulation to epigenetics, metabolism and beyond. *Nat Rev Mol Cell Biol.* 2015;16(4):258-264.
30. Baeza J, Lawton AJ, Fan J, et al. Revealing Dynamic Protein Acetylation across Subcellular Compartments. *J Proteome Res.* 2020;19(6):2404-2418.
31. Jaramillo-Martinez V, Urbatsch IL, Ganapathy V. Functional Distinction between Human and Mouse Sodium-Coupled Citrate Transporters and Its Biologic Significance: An Attempt for Structural Basis Using a Homology Modeling Approach. *Chemical Reviews.* 2020.

32. Kopel JJ, Bhutia YD, Sivaprakasam S, Ganapathy V. Consequences of NaCT/SLC13A5/mINDY deficiency: good versus evil, separated only by the blood-brain barrier. *Biochem J.* 2021;478(3):463-486.
33. Matricardi S, De Liso P, Freri E, et al. Neonatal developmental and epileptic encephalopathy due to autosomal recessive variants in SLC13A5 gene. *Epilepsia.* 2020;61(11):2474-2485.
34. Bhutia YD, Kopel JJ, Lawrence JJ, Neugebauer V, Ganapathy V. Plasma Membrane Na(+)-Coupled Citrate Transporter (SLC13A5) and Neonatal Epileptic Encephalopathy. *Molecules.* 2017;22(3).
35. Henke C, Tollner K, van Dijk RM, et al. Disruption of the sodium-dependent citrate transporter SLC13A5 in mice causes alterations in brain citrate levels and neuronal network excitability in the hippocampus. *Neurobiol Dis.* 2020;143:105018.
36. Berg JM, Lee C, Chen L, et al. JAKMIP1, a Novel Regulator of Neuronal Translation, Modulates Synaptic Function and Autistic-like Behaviors in Mouse. *Neuron.* 2015;88(6):1173-1191.
37. Ryan BC, Young NB, Crawley JN, Bodfish JW, Moy SS. Social deficits, stereotypy and early emergence of repetitive behavior in the C58/J inbred mouse strain. *Behav Brain Res.* 2010;208(1):178-188.
38. Fan SZ, Sung CW, Tsai YH, Yeh SR, Lin WS, Wang PY. Nervous System Deletion of Mammalian INDY in Mice Mimics Dietary Restriction-Induced Memory Enhancement. *J Gerontol A Biol Sci Med Sci.* 2021;76(1):50-56.
39. Silverman JL, Yang M, Lord C, Crawley JN. Behavioural phenotyping assays for mouse models of autism. *Nat Rev Neurosci.* 2010;11(7):490-502.

40. Lewis MH, Tanimura Y, Lee LW, Bodfish JW. Animal models of restricted repetitive behavior in autism. *Behav Brain Res.* 2007;176(1):66-74.
41. Leo D, Gainetdinov RR. Transgenic mouse models for ADHD. *Cell Tissue Res.* 2013;354(1):259-271.
42. Sagvolden T, Russell VA, Aase H, Johansen EB, Farshbaf M. Rodent models of attention-deficit/hyperactivity disorder. *Biol Psychiatry.* 2005;57(11):1239-1247.
43. Simons M, Trajkovic K. Neuron-glia communication in the control of oligodendrocyte function and myelin biogenesis. *J Cell Sci.* 2006;119(Pt 21):4381-4389.
44. Namboodiri AM, Peethambaran A, Mathew R, et al. Canavan disease and the role of N-acetylaspartate in myelin synthesis. *Mol Cell Endocrinol.* 2006;252(1-2):216-223.
45. Jiang Y, Johnson GA. Microscopic diffusion tensor atlas of the mouse brain. *Neuroimage.* 2011;56(3):1235-1243.
46. Harms RL, Fritz FJ, Tobisch A, Goebel R, Roebroeck A. Robust and fast nonlinear optimization of diffusion MRI microstructure models. *Neuroimage.* 2017;155:82-96.
47. Alexander DC, Hubbard PL, Hall MG, et al. Orientationally invariant indices of axon diameter and density from diffusion MRI. *Neuroimage.* 2010;52(4):1374-1389.
48. Barnett BR, Torres-Velazquez M, Yi SY, et al. Sex-specific deficits in neurite density and white matter integrity are associated with targeted disruption of exon 2 of the Disc1 gene in the rat. *Transl Psychiatry.* 2019;9(1):82.
49. Pehar M, O'Riordan KJ, Burns-Cusato M, et al. Altered longevity-assurance activity of p53:p44 in the mouse causes memory loss, neurodegeneration and premature death. *Aging Cell.* 2010;9(2):174-190.

50. Goebbels S, Oltrogge JH, Kemper R, et al. Elevated phosphatidylinositol 3,4,5-trisphosphate in glia triggers cell-autonomous membrane wrapping and myelination. *J Neurosci.* 2010;30(26):8953-8964.
51. Frost DC, Greer T, Li L. High-resolution enabled 12-plex DiLeu isobaric tags for quantitative proteomics. *Anal Chem.* 2015;87(3):1646-1654.
52. Tyanova S, Temu T, Cox J. The MaxQuant computational platform for mass spectrometry-based shotgun proteomics. *Nat Protoc.* 2016;11(12):2301-2319.
53. Tyanova S, Temu T, Sinitcyn P, et al. The Perseus computational platform for comprehensive analysis of (prote)omics data. *Nat Methods.* 2016;13(9):731-740.
54. *enrichplot: Visualization of Functional Enrichment Result* [computer program]. Version R package version 1.8.12020.

# Figure legends

**Figure 1 SLC13A5 nTg mice overexpress SLC13A5 in neurons.** (**A**) mRNA expression of *SLC13A5* in adult neurons. Mice are 6 to 9-month-old females. (**B**) Paraffin-embedded brain immunostaining. Mice are 7-month-old females.

**Figure 2 SLC13A5 nTg mice exhibit jumping stereotypy and autistic-like behaviors.** (**A**) Number of jumps in a 50-second period. WT, $n = 4$; nTg female, $n = 4$; nTg male, $n = 4$. $p < 0.0001$ for both WT vs. SLC13A5 nTg female and WT vs. SLC13A5 nTg male comparisons via one-way ANOVA ($F$ statistic = 57.41) with Tukey's multiple comparison test. (**B**) Open field (OF) assay. WT, $n = 10$; Tg, $n = 10$; equal males/females. Total distance: $p = 0.0158$ via two-way ANOVA (genotype *x* sex; $F$ statistic = 7.291 for genotype factor). Distance in centroid: $p = 0.0005$ via two-way ANOVA (genotype *x* sex; $F$ statistic = 18.73 for genotype factor). Ambulatory time: $p = 0.0023$ via two-way ANOVA (genotype *x* sex; $F$ statistic = 13.16 for genotype factor). (**C**) Light-dark (LD) exploration. WT, $n = 10$; Tg, $n = 10$; equal males/females. Light entries: $p = 0.0302$ via two-way ANOVA (genotype *x* sex; $F$ statistic = 5.654 for genotype factor). (**D**) Marble burying (MB) assay. WT, $n = 10$; Tg, $n = 10$; equal males/females. Total: $p = 0.0053$ via two-way ANOVA (genotype *x* sex; $F$ statistic = 10.420 for genotype factor). 50-99%: $p = 0.0042$ via two-way ANOVA (genotype *x* sex; $F$ statistic = 11.160 for genotype factor). (**E**) Novel object recognition (NOR).

WT, *n* = 10; Tg, *n* = 10; equal males/females. Investigation time (novel object): *p* = 0.0114 via two-way ANOVA (genotype *x* sex; *F* statistic = 8.172 for genotype factor). Investigation time (all objects): *p* = 0.0230 via two-way ANOVA (genotype *x* sex; *F* statistic = 6.325 for genotype factor). (**F**) Fear conditioning (FC). WT, *n* = 10; Tg, *n* = 10; equal males/females. Day 2 (challenge): *p* = 0.0147 via two-way ANOVA (genotype *x* sex; *F* statistic = 7.479 for genotype factor). (**G**) Social interaction (SI) assay. WT, *n* = 8 with 3 females and 5 males; Tg, *n* = 10, equal males/females. WT Sociability: *p* = 0.0007 via two-way ANOVA (mouse/empty *x* sex; *F* statistic = 20.520 for mouse/empty factor). SLC13A5 nTg Sociability: *p* < 0.0001 via two-way ANOVA (mouse/empty *x* sex; *F* statistic = 79.49 for mouse/empty factor). WT Recognition: *p* = 0.0003 via two-way ANOVA (familiar/novel *x* sex; *F* statistic = 24.61 for familiar/novel factor). All data are from mice at 4-7 months of age.

**Figure 3 SLC13A5 nTg mice have altered white matter integrity and synaptic plasticity.** (**A**) *Ex vivo* diffusion-weighted imaging of male WT and SLC13A5 nTg mice at 4 months old, *n* = 6 mice per genotype. Fractional anisotropy (FA) and mean diffusivity (MD) were calculated from a region of interest (ROI) analysis using diffusion tensor imaging (DTI) modeling while EC and IC parameters were calculated from a ROI analysis using ActiveAx modeling. Statistical testing was conducted using an unpaired *t*-test with Benjamini-Hochberg procedure with a false discovery rate (FDR) = 0.05. The *t* statistics and corrected *p*-values are as follows: FA left hippocampus (2.243; 0.0487), FA right amygdala (4.703; 0.0013), FA left amygdala (5.118; 0.0013), EC left hippocampus (3.026; 0.0382), IC right amygdala (2.487; 0.0321), IC left amygdala (2.749; 0.0321), IC right corpus callosum (2.693; 0.0321). (**B**) Whole-brain voxel-wise tract-based spatial statistics analysis of DWI in panel A. Colored voxels are statistically different between WT and SLC13A5 nTg ($p < 0.05$). (**C**) Transmission electron microscopy (TEM) of the left hippocampal dentate gyrus stratum moleculare layer. Axon diameter: each data point represents one animal, *p* = 0.0640 via an unpaired *t*-test (*t* statistic = 2.540). G-ratio vs. axon diameter: Best-fit lines were constructed using simple linear regression with the following equations: WT: $y = 0.164x + 0.606$; SLC13A5 nTg: $y = 0.116x + 0.662$. The slopes of the WT and SLC13A5 nTg regression lines were found to be unequal (*F* statistic = 4.167; *p* = 0.0426). Data are from *n* = 3 mice per genotype (male at 4 months old). (**D**) Theta-burst (3X) long-term potentiation in hippocampal brain slices. Data are mean ± SEM. Mice are 3-4 months old. (**E**) NMDA-induced long-term depression in hippocampal brain slices. Data are mean ± SEM. *p* = 0.0202 via an unpaired *t*-test (*t* statistic = 2.644) of the average potentiation value in the last 10 minutes, *n* = 7 WT (from 2 male and 2 female mice) and 8 SLC13A5 nTg (from 2 male and 3 female mice) slices. Mice are 3-4 months old. (**F**) Golgi staining of CA1 pyramidal neuron apical dendrites (secondary branches). Representative images along with unbiased dendrite and spine reconstructions are shown. Data are shown with each data point representing one animal. Spine volume: *p* = 0.0324 via an unpaired *t*-test (*t* statistic = 2.527), *n* = 6 mice per genotype (3 males, 3 females; one SLC13A5 nTg male outlier removed) at 3 months old.

**Figure 4 Primary cortical neurons from SLC13A5 nTg mice have normal morphology but reduced synapse formation and increased spontaneous activity.** (**A**) Morphologic assessment of cultured neurons at 15 days *in vitro* (DIV). Phalloidin staining (left) and unbiased computer-driven reconstruction (right) are shown along with quantification from *n* = 3 embryos per genotype. Data are mean ± SEM (Sholl analysis) or SD (spine density and volume) with each data point representing one embryo. (**B**)

Immunostaining of cultured neurons for pre-synaptic marker Syn1 and post-synaptic marker Psd-95 at 15 DIV. Puncta were fit with 2 μm spots and normalized to neuron volume, and spots co-localized if they were within 1 μm of each other. Data are shown with each data point representing one embryo, *n* = 4 WT and *n* = 3 SLC13A5 nTg. Statistical testing was conducted via unpaired *t*-test with the *t* statistics and *p*-values as follows: Syn-1 (3.817; 0.0124), Psd-95 (6.203; 0.0016), co-localized (5.931; 0.0019). (**C**) Multi-electrode array spontaneous activity. Left: histogram showing the number of active electrodes per network expressed as the relative frequency in percent. The vertical line demarks 8 active electrodes, which is the minimum value required to be considered a mature network. Statistical testing was conducted via the Mann-Whitney test comparing frequency distributions at each DIV with Mann-Whitney *U* values and *p*-values as follows: DIV7 (108.5; 0.0001), DIV14 (155; 0.0061), DIV 21 (138.5; 0.0020), DIV 28 (110; 0.0002). Right: spontaneous activity measured by mean firing rate, burst frequency, network burst frequency, and synchronicity index. Each data point is an independent network of cultured neurons and exhibits at least 8 of 16 active electrodes. Statistical testing was conducted via mixed effects analysis (DIV *x* genotype) with Sidak's multiple comparison test. DIV7 data were excluded from analysis due to the lack of WT values. Test details are as follows, listing the *F* statistics for the genotype factor and adjusted *p*-values from multiple comparison testing: mean firing rate (8.956; DIV14, 0.0001; DIV 21, 0.0303), burst frequency (5.505; DIV14, 0.0013; DIV 21, 0.0178), network burst frequency (3.789; DIV14, 0.0013; DIV28, 0.0346), and network synchronicity (6.745; DIV14, 0.0160). Data are from 3 WT and 7 SLC13A5 nTg embryos.

**Figure 5 Primary hippocampal neurons from SLC13A5 nTg mice have normal morphology, synaptic density, and spontaneous activity.** (**A**) Morphologic assessment of cultured neurons at 15 days *in vitro* (DIV). Phalloidin staining (left) and unbiased computer-driven reconstruction (right) are shown along with quantification from *n* = 3 WT and 4 SLC13A5 nTg embryos. Data are mean ± SEM (Sholl analysis) or SD (spine density and volume) with each data point representing one embryo. (**B**) Immunostaining of cultured neurons for pre-synaptic marker Syn1 and post-synaptic marker Psd-95 at 15 DIV. Puncta were fit with 2 μm spots and normalized to neuron volume, and spots co-localized if they were within 1 μm of each other. Data are shown with each data point representing one embryo, *n* = 4 WT and *n* = 3 SLC13A5 nTg. Syn-1: *p* = 0.0338 via an unpaired *t*-test (*t* statistic = 2.900). (**C**) Multi-electrode array spontaneous activity. Left: histogram showing the number of active electrodes per network expressed as the relative frequency in percent. The vertical line demarks 8 active electrodes, which is the minimum value required to be considered a mature network. DIV7 *p*-value = 0.0328 via the Mann-Whitney test comparing frequency distributions (Mann-Whitney *U* = 185). Right: spontaneous activity measured by mean firing rate, burst frequency, network burst frequency, and synchronicity index. Each data point is an independent network of cultured neurons and exhibits at least 8 of 16 active electrodes. Data are from 3 WT and 7 SLC13A5 nTg embryos.

**Figure 6 SLC13A5 nTg mice display global proteomic changes in the hippocampus and cortex.** (**A**) Volcano plots displaying all quantified proteins in SLC13A5 nTg hippocampus (left) and cortex (right) compared with WT controls. Statistically significantly changed proteins are shown in green (607 in hippocampus and 107 in cortex; $p < 0.05$ via Fisher's method) with all other proteins in grey. *n* = 4 male mice per genotype at 4-7 months of age. (**B**) Histogram and overlaid Gaussian distribution showing the

distribution of all proteins' $\log_2$ fold changes from WT in hippocampus and cortex. A box and whisker plot is shown above with the box representing $25^{th}/75^{th}$ percentiles, middle line representing mean, and whiskers representing $1^{st}/99^{th}$ percentiles. $p < 0.0001$ via the Kolmogorov-Smirnov test (Kolmogorov-Smirnov $D = 0.1496$). (**C**) Significant protein overlap between the hippocampus and cortex. All proteins highlighted in green shown in panel A are included. The heat map shows the expression profile of the 37 overlapping proteins between hippocampus and cortex. (**D**) The fold enrichment of KEGG pathways that were found to be enriched as determined from significant proteins in the hippocampus and cortex compared with WT controls. The top 10 categories sorted by enrichment score are shown that have been filtered by a FDR score of 0.05. (**E**) Gene-network plots of significantly changed proteins in the SLC13A5 nTg hippocampus and cortex. Plots were constructed using an overrepresentation analysis using the gene ontology cellular component function database. Results were filtered by a FDR score of 0.05. The top 5 results are shown for the hippocampus (due to space limitations); for the cortex, all significant categories are displayed. The dot size of each network category is scaled by the number of overlapping proteins within the category.

**Figure 7 SLC13A5 nTg mice display changes in the stoichiometry of acetylation in the hippocampus and cortex.** (**A**) Volcano plots displaying all quantified acetylpeptides in the SLC13A5 nTg versus WT hippocampus (top) and cortex (bottom) across the three subcellular fractions (cytosolic, nuclear/membrane, and chromatin-associated). Change in acetylation stoichiometry ($\Delta$ acetyl stoichiometry) is calculated as the SLC13A5 nTg stoichiometry value less the WT stoichiometry value. Statistically significant acetylpeptides ($p < 0.05$) are shown in green with all other acetylpeptides in grey. $n = 4$ male mice per genotype at 4 months of age. (**B**) Overlap of the statistically significant acetylpeptides across the three subcellular fractions in both the hippocampus and cortex. (**C**) Overlap between the hippocampus and cortex of all the statistically significant acetylpeptides (combined from the three subcellular fractions). A heat map of the 9 overlapping acetylpeptides between the two tissue types is shown. (**D**) The fold enrichment of KEGG pathways determined from proteins harboring the acetylation sites that were significantly changed from WT in the hippocampus and cortex. The top 10 categories sorted by enrichment score are shown that have been filtered by a FDR score of 0.05. (**E**) Gene-network plots of proteins harboring the acetylation sites that were significantly changed from WT in the hippocampus and cortex. Plots constructed using an overrepresentation analysis using the gene ontology cellular component function database. The dot size of each network category is scaled by the number of overlapping proteins within the category. The top 10 categories sorted by enrichment score are shown that have been filtered by a FDR score of 0.05. Since proteins could be found in multiple fractions and potentially acetylated on multiple lysine sites, the $\Delta$ acetyl stoichiometry value displayed in the network plot is as follows: (1) If the acetylpeptide was detected in multiple subcellular fractions, the fraction selected for illustration was prioritized as follows: cytoplasmic, nuclear/membrane, then chromatin-associated. (2) If multiple sites per protein exhibited significantly changed acetyl stoichiometry, the lowest number lysine residue was selected for illustration.

**Figure 8 SLC13A5 nTg hippocampus but not cortex displays overlap in the proteome and acetyl-proteome.** (**A**) Venn diagrams showing the overlap between the proteins with significantly different expression compared to WT (proteome) and proteins harboring the acetylation sites exhibiting significant changes from WT (acetyl-proteome) in the hippocampus and cortex, respectively. (**B**) Proteins from one overlapping gene ontology cellular component category shown in *Figure 6E* and *Figure 7E* (myelin sheath) with denoted changes at the level of the proteome or acetyl-proteome. The following protein acetylation sites were detected in multiple fractions thus was selected for illustrative purposes: Calm1, K31 in nuclear/membrane; Syn1, K318 in cytoplasmic.

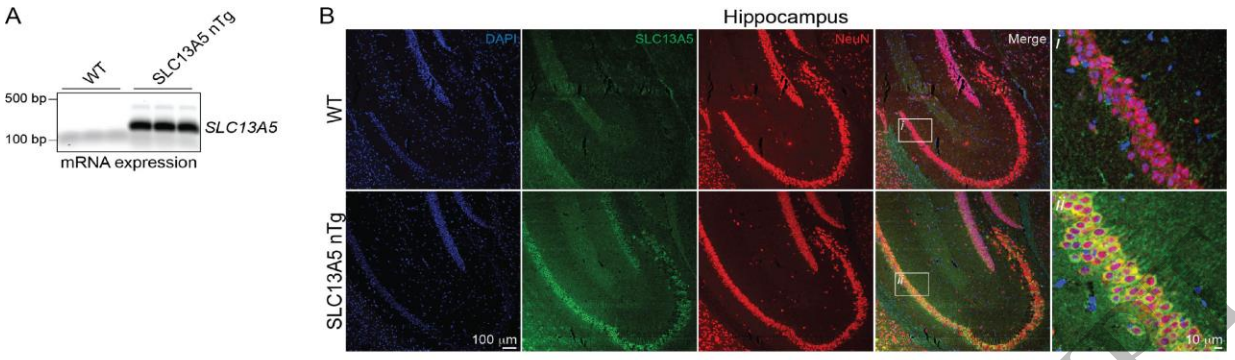






**Figure 1**
**162x229 mm (0.6 x DPI)**

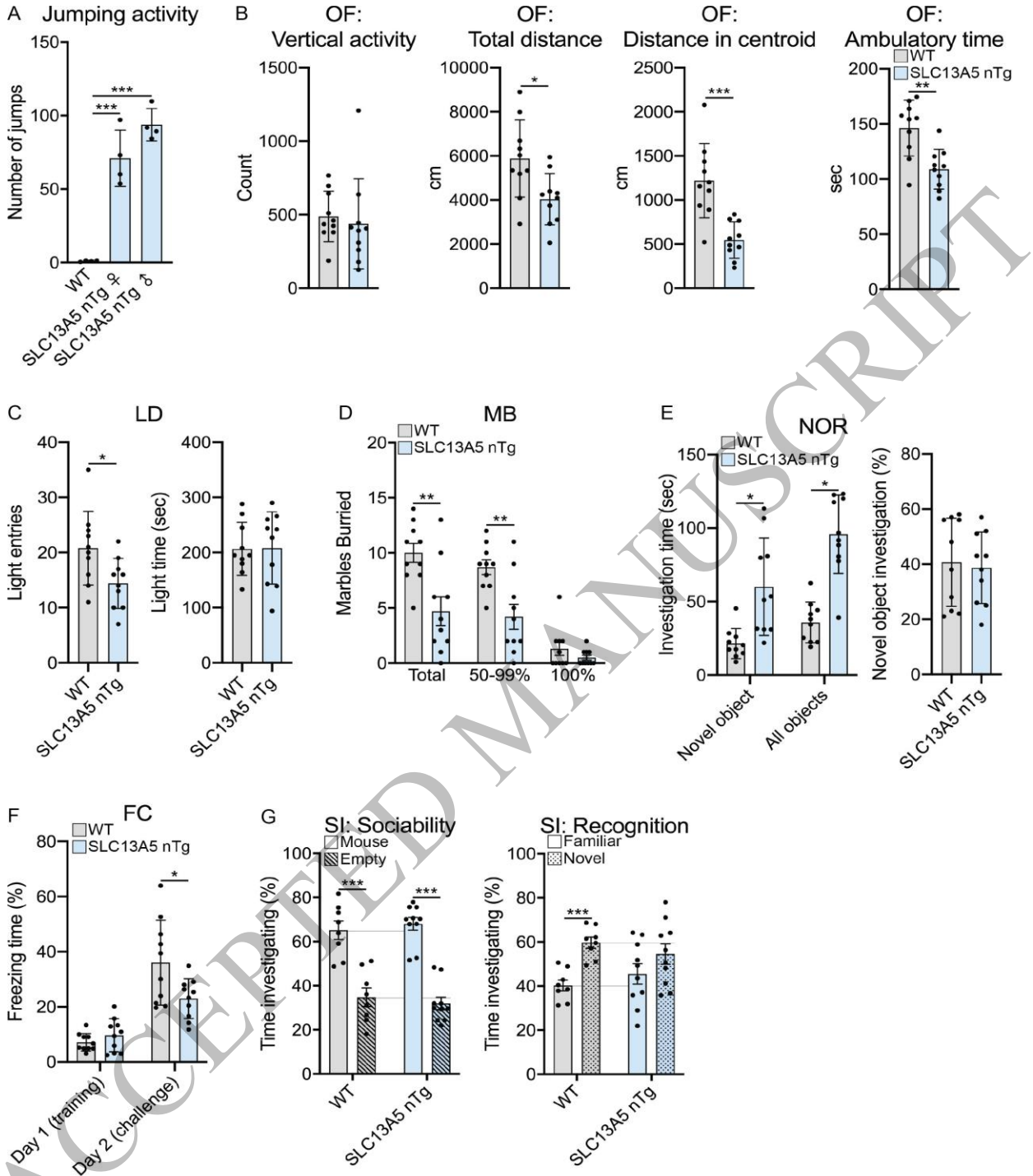


**Figure 2**
**162x229 mm (0.6 x DPI)**

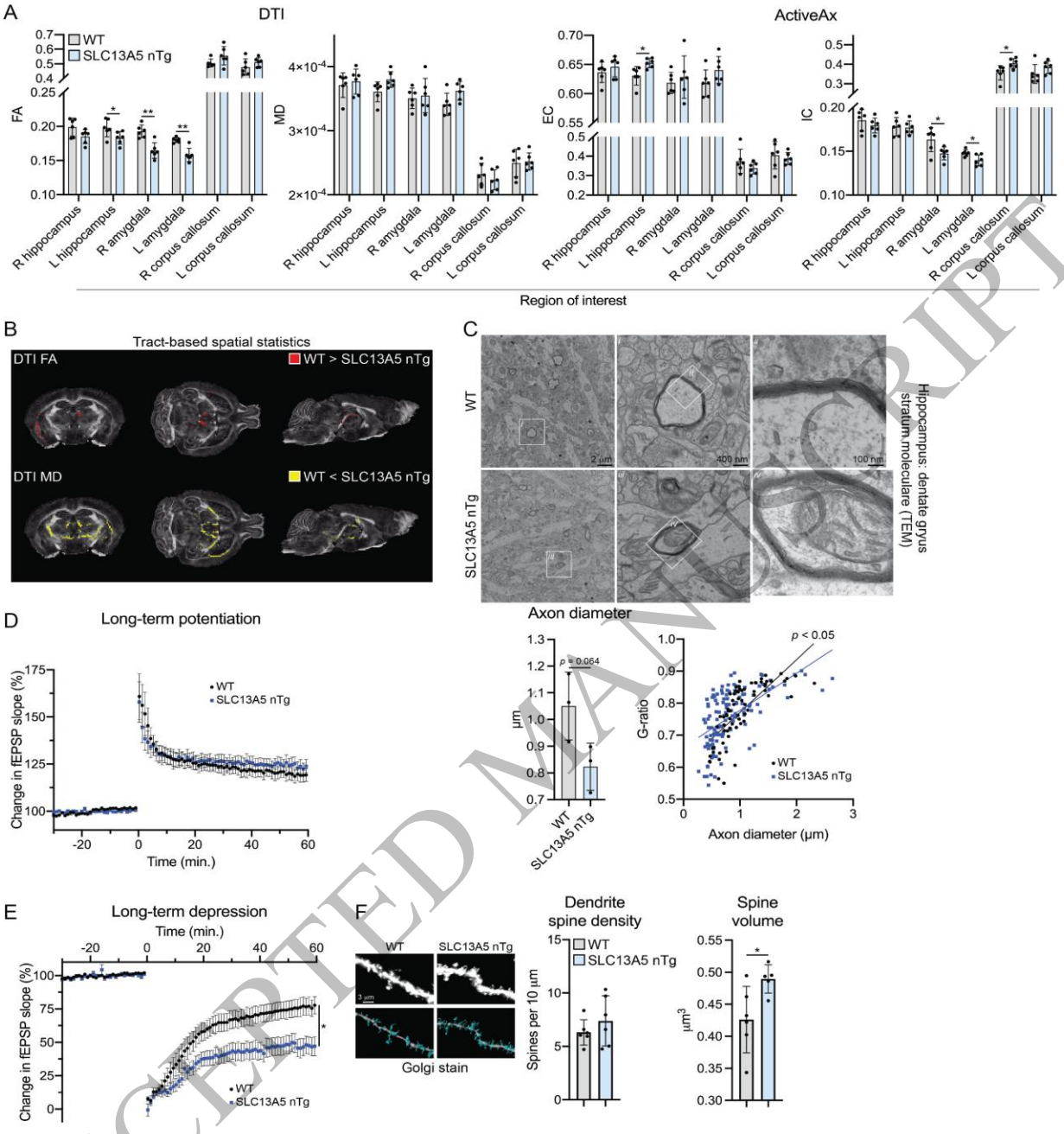


**Figure 3**
**162x229 mm (0.6 x DPI)**

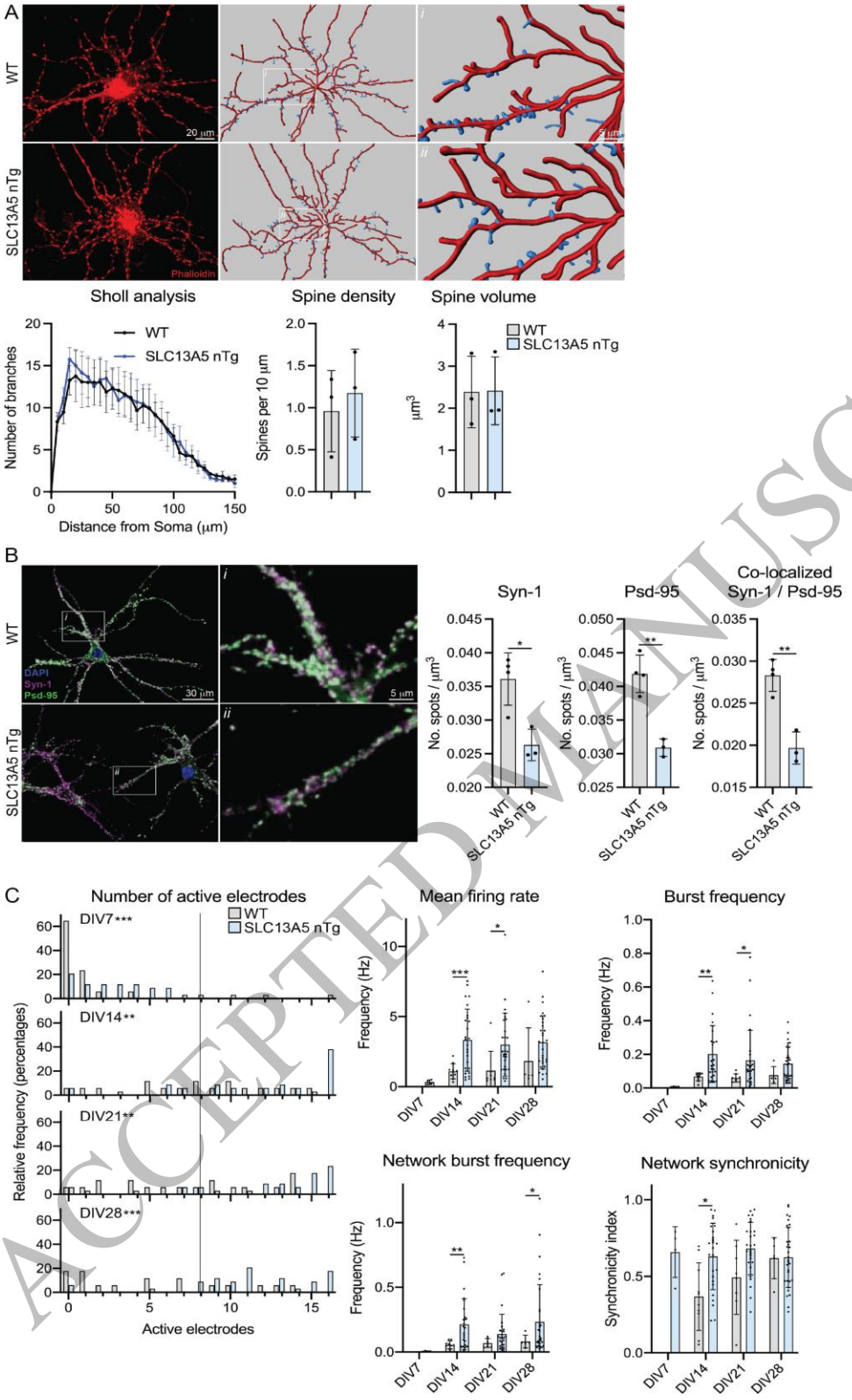


**Figure 4**
**162x229 mm (0.6 x DPI)**

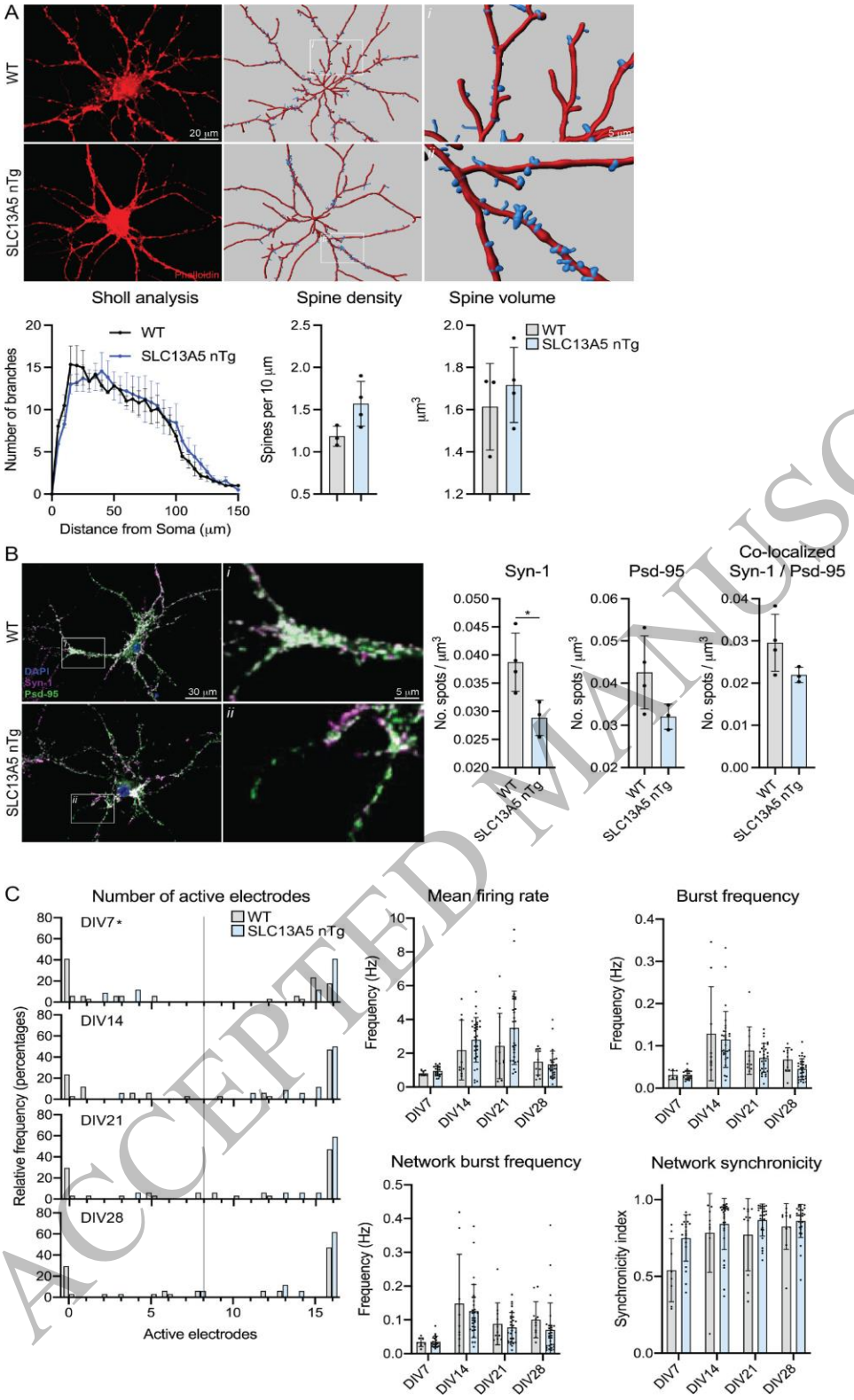


**Figure 5**
**162x229 mm (0.6 x DPI)**

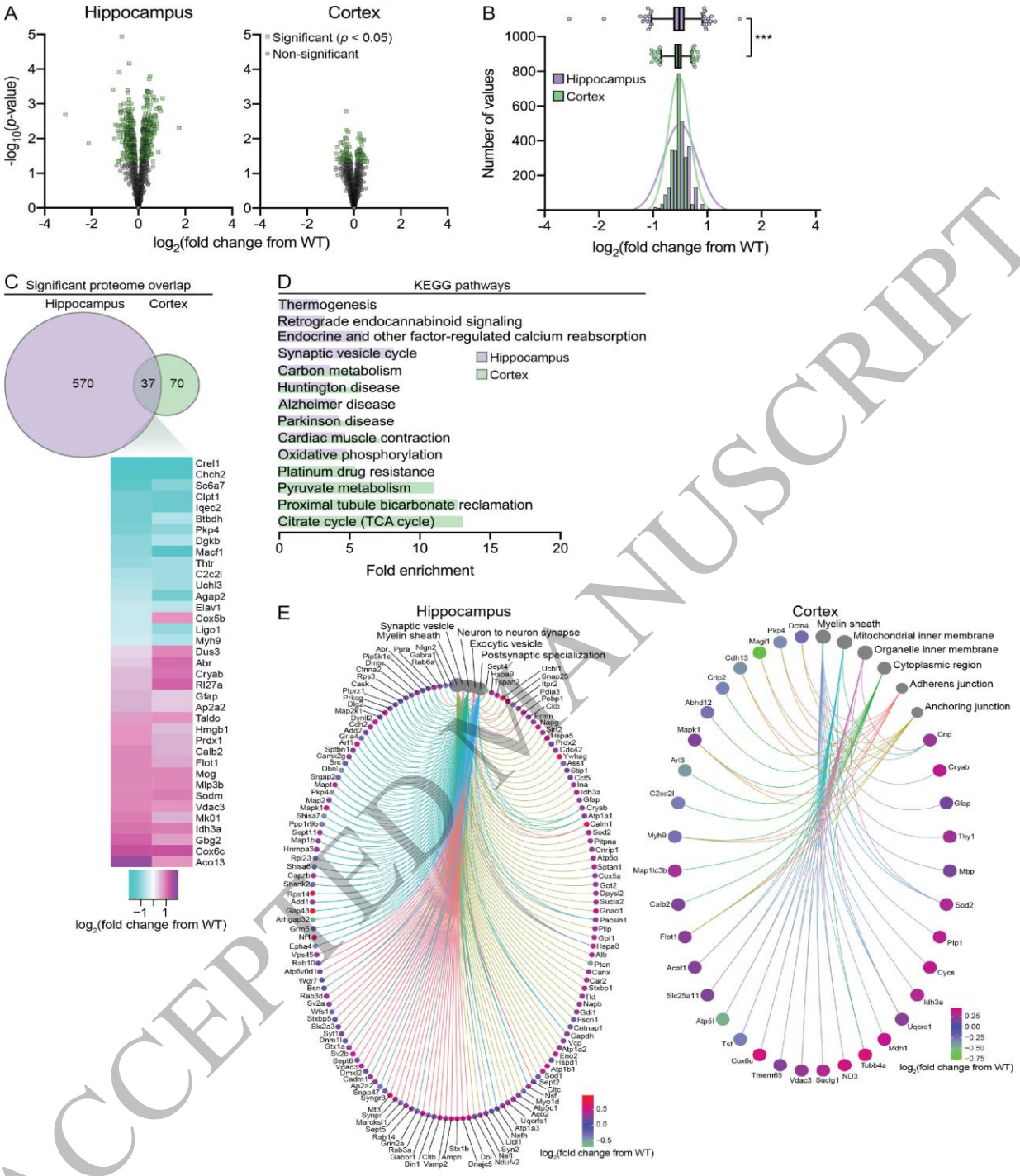


**Figure 6**
**162x229 mm (0.6 x DPI)**

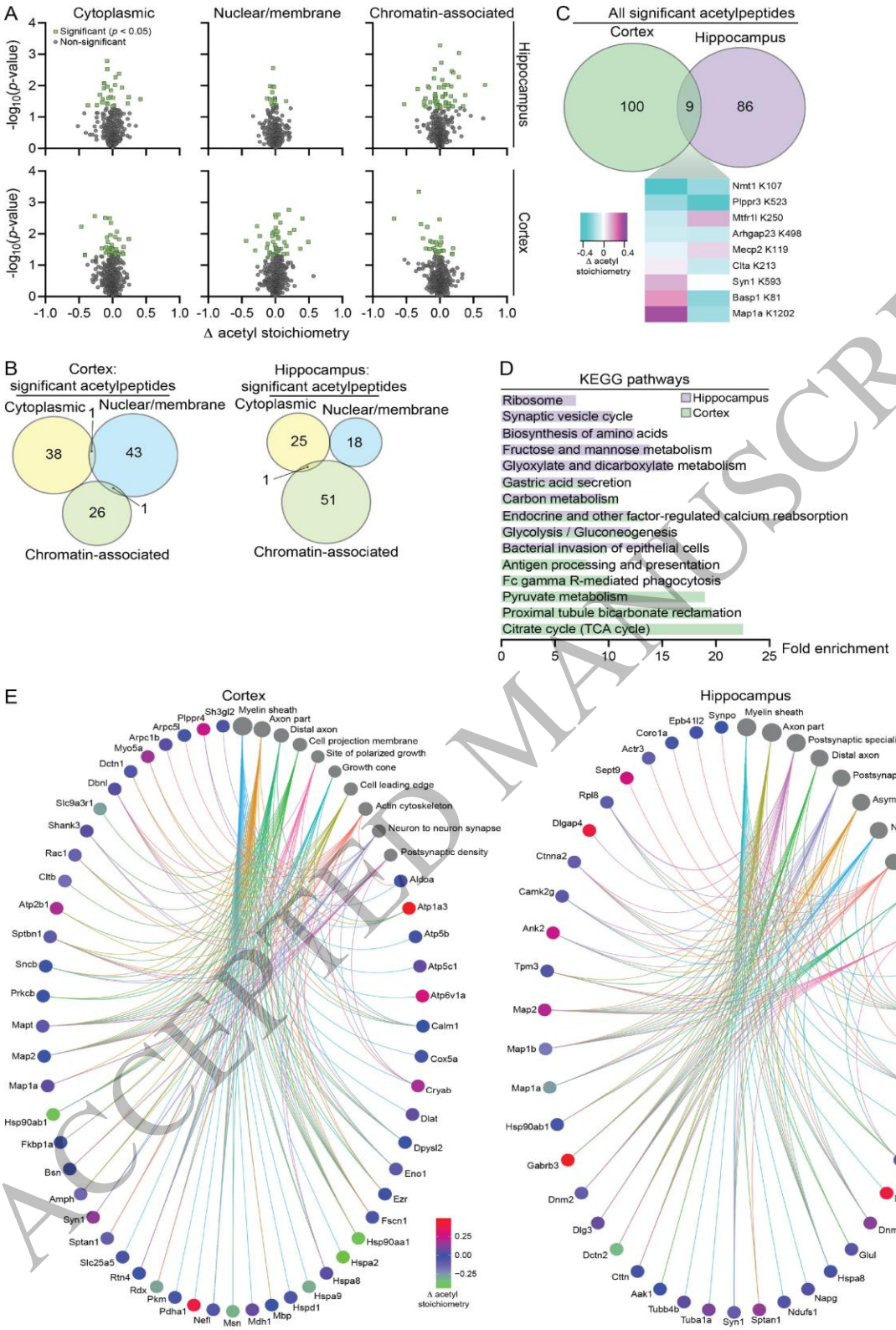


**Figure 7**
**162x229 mm (0.6 x DPI)**

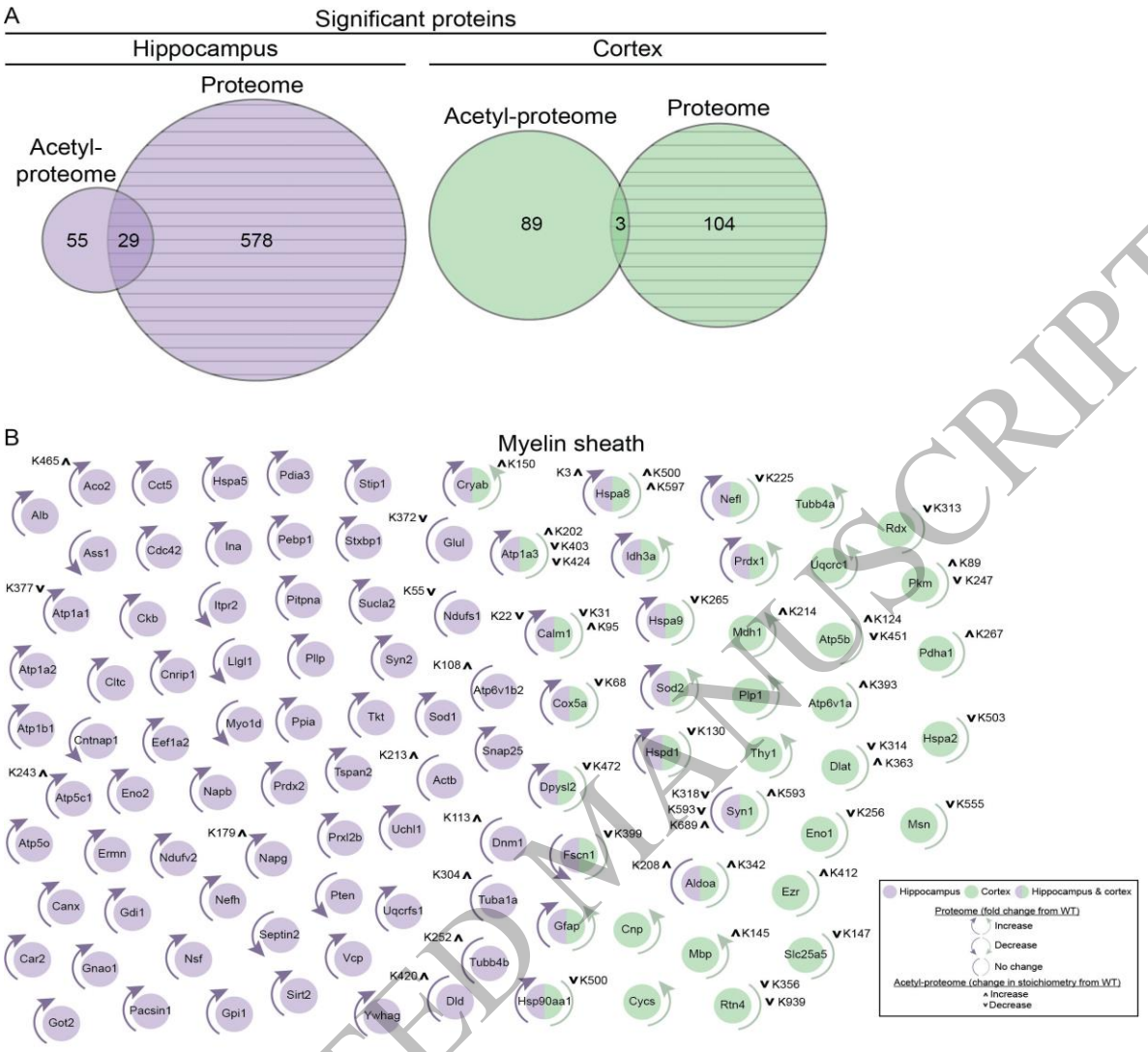


**Figure 8**
**162x229 mm (0.6 x DPI)**

Rigby *et al*. report that forebrain neuron-specific overexpression of SLC13A5, the plasma membrane sodium/citrate symporter, results in an autistic-like phenotype in the mouse with disrupted white matter integrity, altered synaptic development, and widespread proteomic and acetyl-proteomic adaptations. This study reinforces a link between aberrant intracellular citrate/acetyl-CoA flux and autism.